

The Path to COVIS: a review of acoustic imaging of hydrothermal flow regimes

Karen G. Bemis^{1,c}, Deborah Silver², Guangyu Xu¹, Russ Light³, Darrell Jackson³, Christopher Jones³, Sedat Ozer⁴, Li Liu²

¹ Department of Marine and Coastal Sciences, Rutgers The State University of New Jersey, New Brunswick, NJ 08901; bemis@rci.rutgers.edu

²Department of Electrical and Computer Engineering, Rutgers The State University of New Jersey, Piscataway, NJ 08855

³Applied Physics Laboratory, University of Washington, Seattle, WA 98105

⁴Department of Computer Science, University of Virginia, Charlottesville, VA 22904

^ccorresponding author, bemis@rci.rutgers.edu.

ABSTRACT

Acoustic imaging of hydrothermal flow regimes started with the incidental recognition of a plume on a routine sonar scan for obstacles in the path of the human-occupied submersible ALVIN. Developments in sonar engineering, acoustic data processing and scientific visualization have been combined to develop technology which can effectively capture the behavior of focused and diffuse hydrothermal discharge. This paper traces the development of these acoustic imaging techniques for hydrothermal flow regimes from their conception through to the development of the Cabled Observatory Vent Imaging Sonar (COVIS). COVIS has monitored such flow eight times a day for several years. Successful acoustic techniques for estimating plume entrainment, bending, vertical rise, volume flux, and heat flux are presented as is the state-of-the-art in diffuse flow detection.

Keywords: Acoustic imaging, Hydrothermal fields, Heat transport, Heat conduction, Visualization, Mid-ocean ridges, Pacific Ocean, Juan de Fuca Ridge, Main Endeavour Field, Grotto

1 Introduction

While scanning the seafloor terrain for obstacles, a 37kHz sonar on ALVIN intersected hydrothermal plumes at the EPR (Palmer, et al., 1986). In this 1984 survey of the Feather Duster vent field ($10^{\circ}56'N$ EPR), photographs of sonar range-finding showed a variety of targets, including pillow lava forms, the rim of a lava lake and hydrothermal plumes (Palmer et al., 1986). In observations reported by Palmer et al. (1986), the hydrothermal plume targets are differentiated from the underlying sulfide mound based on the estimated dimensions of the target (7-10 m wide), the known location and dimensions (4-5 m wide) of the sulfide mounds relative to the submersible, the apparent radial stretching due to the vertical extent of the target (an implied 16 m vertical extent where chimneys are generally less than 4m), and the inferred rising and expanding behavior of plume(s). Thus began a series of studies leading to the development of specialized acoustic imaging techniques for hydrothermal plumes.

1.1 Importance of hydrothermal systems

Seafloor hydrothermal systems form a fundamental part of magmatic systems, wherein seawater percolates downward into the deep crust, absorbs volcanic heat, rises buoyantly, and discharges at the seafloor (German and Von Damm, 2006). Discharge occurs both as high temperature fluids exiting in a focused manner through chimneys and flanges and as lower temperature fluids exiting diffusely through mounds, faults, and cracks in the seafloor.

On a global scale, such hydrothermal discharge is important for several reasons. First, the convective flow of the mid-oceanic ridge hydrothermal system is responsible for ~33% of the transfer of heat from the Earth's crust to the ocean (German and Von Damm, 2006). Second, the impact of hydrothermal discharge on ocean chemistry is on the scale of riverine impacts for many chemical processes (Bickle and Elderfield, 2004). Third, the heat and chemical output of hydrothermal discharge supports a local ecosystem through chemosynthesis based on reduced gases (e.g., H₂S and CH₄) carried by the hydrothermal fluids (Govenar, 2012).

Measuring the fluxes of heat and chemicals transported by hydrothermal systems from the mantle to the ocean provides significant logistical and measurement challenges (Rona et al., 2015, this issue). Approaches to measuring fluxes have either focused on detailed accounting for discharge sites (e.g., black smokers, diffuse discharge) on or near the seafloor or attempted to capture the integrated flux (e.g., buoyant plume and neutrally-buoyant plume) high in the water column (Baker, 2007). The need for a large number of measurements across a significant area (or volume) limits the accuracy of both approaches. This motivates the development of remote sensing techniques that can capture areas and volumes of flows, flow rates and possibly temperatures rapidly (if not instantaneously) over large (or at least larger) distances. The acoustic imaging techniques discussed herein are one such technique.

1.2 Field measurements (non-acoustic) for estimating heat flux

In general, heat flux can be estimated by measuring the amount of heat (temperature) flowing through a given area. If accounting for a collection of discharge sites, the obvious approach relies on direct measurement of temperature, discharge or orifice area, and exit velocity. The integrated (water column) approaches measure the spatial variations of flow velocity and/or heat content to estimate heat flux. Two measurement challenges are common to both approaches: (1) measuring flow rates whether at a black smoker, above a diffuse discharge site, or in the plume rising above such sites and (2) identifying and delimiting accurately the areas through which such flow occurs.

The attempt to quantify flow rates began with the first discoveries of hydrothermal vents discharging hot water into the ocean on mid-oceanic ridges (Corliss et al., 1979; McDonald et al., 1980; Converse et al., 1984). These early efforts used vane-type or turbine flowmeters and video-captured particle motions to estimate vertical rise rates (Corliss et al., 1979; McDonald et al., 1980; Converse et al., 1984). Later studies combined video with graded meter sticks or backgrounds, used increasingly sophisticated software for video analysis, or modified flowmeters to reduce clogging to increase reliable accuracy (e.g., Rona and Trivett, 1992; Crone et al., 2008; Ramondenc et al., 2006). Temperature arrays in a variety of configurations have also been introduced to estimate flux or flow rates based on spatial variations in plumes (vertically) and diffuse discharge (horizontally) (e.g., Little et al., 1987; Bemis et al., 1993; Bates et al., 2010). Nevertheless, achieving considerable spatial coverage with these spot measurements takes significant time, and high degrees of variability prevent accurate use of extrapolation. Alternative water column approaches, such as towing CTDs through the plumes, also lack synchronicity and cannot unambiguously attribute fluxes to a single vent or vent cluster due to the complexities of ocean currents (e.g., Baker and Massoth, 1987; Viers et al., 2006).

The measurement of areas for heat flux estimation presents similar challenges. Accurate measurement of the area of a single black smoker orifice depends on good video of the exit point (tricky with the high velocity and high temperature flow in the way). Furthermore, determining the total number of black smokers traditionally requires a systematic (and time consuming) survey of the relevant region. Similarly, diffuse discharge areas are traditionally located by video survey. Recent developments of photo mosaic and photogrammetric techniques are improving the accuracy of such surveys (Kwasnitschka et al., 2013; Barreyre et al., 2012); however, significant underwater vehicle time is still required to collect the video data.

Beyond the quantitative estimation of heat flux, efficient and accurate visualization of the behavior of underwater hydrothermal systems has the potential to support qualitative assessment of the spatial and temporal variability of hydrothermal discharge. Data acquisition techniques, which are suited to imaging and potentially relevant to studying hydrothermal discharge, include both optical and acoustic imaging. As discussed above, non-imaging data acquisition methods generally do not supply sufficient spatial coverage to efficiently describe or image any significant portion of a hydrothermal system (even a single vent can have a 10-30 m diameter footprint on the seafloor and the discharging fluids can rise as plumes for hundreds of meters). Optical imaging is challenged by the rapid attenuation and high scattering rates of light in seawater (Jaffe, 1990; Kocak et al., 2008). Optical imaging of hydrothermal plumes is impractical: video and photographs rarely show features more than 10-20 m from the camera. Close-up detection of diffuse flow by optical imaging is feasible (Smart et al., 2013; Mittelstaedt et al., 2012); broad imaging of the seafloor distribution of discharge by photogrammatic or photomosaic methods is also feasible (Kwasnitschka et al., 2013; Barreyre et al., 2012). However, both require considerable underwater vehicle time. In contrast, acoustic imaging offers the ability to detect discharge over areas from 10's to 100' m² with only minutes of imaging from a single location.

1.3 Advantages of acoustic imaging

Palmer et al. (1986) recognized that acoustic imaging had the potential for acquiring measurements over a broader area (>10m² rather than <0.1-1 m² for spot and small volume measurements) in a relatively short time interval (seconds to minutes rather than the minutes to hours of deep towing or vehicle surveys). Furthermore, acoustic techniques for determining flow rates, temperature fluctuations, and particle concentrations already existed or were being developed (Weston, 1959; Orr and Hess, 1978; Jackson and Dworski, 1992). In short, the anticipated advantages of acoustic imaging included the definition of plume boundaries to estimate entrainment and injection into the ocean (useful as the dilute plume is difficult to see at 10's of meters above its source with cameras), the estimation of particulate motion along sonar imaging direction with potential to estimate internal plume motion (that is flow rates and fluxes), and the estimation of particle concentration to investigate suspended particle distribution (Palmer et al., 1986).

In this paper, we will establish that acoustic imaging has three advantages: (1) estimation of the vertical velocity distribution within the lower buoyant plume provides volume flux and heat flux estimates for an integrated portion of the hydrothermal site; (2) a modification of the acoustic imaging approach can detect diffuse discharge over a significant (hundreds of m²) area; and (3) the remote sensing nature of acoustic imaging data combined with visualization techniques effectively captures the quantitative distribution of both buoyant plumes and diffuse discharge over a significant (hundreds of m²) area.

1.4 Visualization of hydrothermal discharge

While the development of acoustic imaging was mainly motivated by its ability to quantify properties of hydrothermal discharge, acoustic imaging also has the potential to communicate aspects of the spatial distribution (and temporal variation) in a 3D visual mode. Visualization of the acoustic data facilitates the perception and quantification of spatial and dynamic variations in hydrothermal discharge. As a result, the development and application of 3D visualization techniques accompanied the development of the acoustic techniques. The visualization process starts with data acquisition, proceeds to data processing and ends with visual rendering techniques; the development of acoustic data processing and illustration methods becomes intertwined with the development of visualization methods. This paper will thus trace the contemporaneous developments in scientific visualization that have enabled both effective presentation and three-dimensional quantitative analysis of the acoustic imaging data.

1.5 Description of this paper

This paper traces the following: (1) the development of acoustic imaging as a tool for exploring hydrothermal plumes from the initial adaptive use of navigation sonar to the use of a sonar specifically designed for attachment to a cabled underwater observatory; and (2) the related development of visualization applications for illustrating and quantifying hydrothermal fluxes. Table 1 presents an overview of the developments discussed in the following sections. Section 2 covers the initial sonar detection of hydrothermal plumes and the mechanisms of scattering enabling detection. Section 3 discusses the acoustical engineering developments. Section 4 details the visualization and quantification developments, including changes in data processing leading to additional scientific information. Section 5 highlights the key scientific results concerning hydrothermal plumes. Section 6 gives a brief overview of COVIS and the scientific information it is capable of acquiring. Section 7 provides some concluding thoughts.

2 Detecting hydrothermal plumes with sonar

Increased reverberation has long been observed in the presence of suspended particulate matter in the water column (e.g., Weston, 1959; Palmer et al., 1986; Medwin and Clay, 1997). In the 1980's, active sonar was developing into a useful tool for the quantitative measurement of ocean dynamics, including the detection of internal wave activity, turbidity currents, pollution, and naturally occurring plumes of a variety of types (see references in Palmer et al., 1986). During deep tow operations in 1980, an upward-looking 23.5 kHz sonar and a 110 kHz side scan sonar captured the rise of bubbly hydrate plumes from the Guaymas Basin in the Gulf of California (Merewether et al., 1985). Soon thereafter (1982-1983), Hay used a standard 200 kHz acoustic sounder from a launch to outline the extent of a buoyant plume from a submarine spring in Cambridge Fjord, Baffin Island (Hay, 1984). The scattering mechanisms for this Arctic spring were inferred as temperature and salinity fluctuations due to turbulent mixing. In 1984, an ALVIN survey of the Feather Duster vent field ($10^{\circ}56'N$ EPR) obtained photographs of a 37 kHz sonar range-finding showing a variety of targets including hydrothermal plumes (Palmer et al., 1986). These detections of various plumes provided scientific justification for a study of the potential mechanism for acoustic scattering and the development of specialized acoustic imaging techniques for hydrothermal plumes (Palmer and Rona, 2005).

2.1 Basic concepts of backscattering and acoustic imaging

Acoustic imaging is an active source acoustic (or sonar) technique. Acoustic techniques are based on the measurement of the energy or strength of sound waves traveling in water (or other media). In general, the magnitude of a sound wave decreases with the distance traveled due to attenuation and spherical spreading, which the combined effect is called the transmission loss. Active source indicates that the sensor both sends out the sound and measures its echo. When the sound

reaches a target composed of many small scatterers, the sound is scattered in all directions. Some portion of the scattered sound then returns to the source; this is called backscatter. Fig. 1A illustrates this process. The potential scatterers in the ocean include gas bubbles, metallic sulfide particles, zooplankton, changes in the sound speed or density of water, and more.

Active sonar sensors can package the transmitter (source of sound) together with, or separately from, the receiver (which records the incoming sound). In applications for detecting hydrothermal plumes, the sonar contains both transmitter and receiver in near proximity (although a variety of configurations have been used as described in section 3). Both temperature fluctuations (which cause sound speed and density variations) and particulates (mostly metallic sulfide particles) cause scattering in hydrothermal plumes (Xu and Di Iorio, 2012; see further discussion in the next section 2.2).

The volume backscatter cross-section σ_b in units of 1/m is the general measure of the backscattering strength regardless of mechanism. Estimation of volume backscattering strength from the raw acoustic signal involves both pre-processing needed for the conversion to volume backscattering strength (e.g., corrections for transmission loss and adjustments based on sonar properties) and additional processing to create a 3D volume from the raw ping structures (which depends on the sonar setup but does not affect the conversion); section 4 discusses the processing of acoustic data in more detail. Recent acoustic data (where calibration data for the sonar source is available) are reported as volume backscattering cross-section (as σ_b in units of 1/m) or, more conventionally, volume backscattering strength (as $10\log_{10}(\sigma_b)$ in units dB). This volume backscattering strength can be readily compared with the predictions made by models of scattering mechanisms without the need to account for specific sonar parameters or transmission loss.

Imaging a plume in three dimensions requires the following: (1) the creation of a narrow beam from the sonar; (2) a means to cover a 3D volume with that beam; and (3) recording the returning sound over a period of time. The 2-way travel time corresponds to the 2-way distance the sound traveled; this use of time for line-of-sight distance is akin to the use of two-way travel time for depth into the lithosphere as used in seismic reflection. In the current (COVIS) technology, the transmitted beam is narrow in the horizontal and wide in the vertical. The receiver forms narrow beams in the vertical by means of digital signal processing. These beams are wide in the vertical. Mechanical rotation of both transmitter and receiver in the vertical (along with recording of the signal over time) allows us to cover a 3D volume.

2.2 Scattering mechanisms in hydrothermal plumes

Initially, the sonar signal (Fig. 2A) was assumed to be backscatter from metallic sulfide particles in the hydrothermal plumes, although alternative scattering mechanisms, including temperature fluctuations, were considered (Palmer et al., 1986). For scattering from metallic sulfide particles, the likelihood of imaging a plume (or the strength of the particulate backscattering intensity) depends on the sonar carrier frequency (37kHz for that first image), the particle size (4-15 um), the particle concentration (5-150 mg/l) and elastic properties, background noise, and the performance level of the sonar. Palmer et al. (1986) estimated that a 37kHz sonar could detect plumes at hundreds of meters and that a 200 kHz sonar could still detect a plume out to 100 m. However, while the acoustic data in this paper demonstrate success in detecting, imaging and quantifying hydrothermal plumes (e.g., Rona et al., 1991; Bemis et al., 2002; Santilli et al., 2004; Rona and Light, 2011), they do not necessarily support the assumption of particulates as the primary scattering mechanism.

Palmer et al. (1986) and many subsequent efforts assumed that turbulent fluctuations ceased to produce significant scattering at heights more than 1 m above the vent. Recent results suggest that this assumption is unjustified. Here we present an overview of scattering due to particulates and due to temperature fluctuations, some simplified predictions, and a summary of the observed backscattering strengths for comparison.

The scattering by particulates has been discussed extensively in the literature (e.g., Palmer et al., 1986; Sheng and Hay, 1988; Xu and Dilorio, 2011). Scattering by a suspension of particles lies in the Rayleigh scattering regime if the particles are small enough such that $k_0 a_s \ll 1$ where $k_0 = 2\pi f_0/c$ is the wavenumber, f_0 is the central frequency of the sonar, c is the speed of sound and a_s is the relevant particle size. For scattering by a suspension of particles, the volume backscatter cross-section σ_b depends on the particle properties (size, concentration and elastic properties) and the frequency of the sonar (Palmer et al., 1986; Sheng and Hay, 1988).

Scattering by temperature fluctuations has also been previously presented (e.g., Oeschger and Goodman, 1996; Duda and Trivett, 1998; Xu and Dilorio, 2011). For scattering by temperature fluctuations, the volume backscattering cross-section σ_b depends on the structure and intensity of the turbulence, on the sensitivity of refractive index and density variations on temperature, and on the sonar frequency.

Fig. 2B compares the observed backscattering strengths from calibrated sonars with model predictions for a few cases: (1) in case 1, we assume particles are of moderate size (15 μm) in a dilute solution (10 mg/l) with only a small temperature anomaly (1°); and (2) in case 2, we assume only very small particles (5 μm) in an even more dilute solution (5 mg/l) but with a larger temperature anomaly (10°). Case 1 characterizes the assumptions of Palmer et al. (1986), while case 2 fits better with the current understanding of particle size (Walker and Baker, 1988), particle concentration (Feely et al., 1994; Mottl and McConachy, 1990), and plume temperature anomalies (Rona et al, 2015).

These predictions for volume backscattering strength show that the predicted scattering due to particulates is much lower than the predicted scattering due to temperature (Fig. 2B). Field observations made by COVIS in 2014 from a hydrothermal plume located on the Endeavour Segment of the Juan de Fuca Ridge in the Northeast Pacific span the predictions of both particulate and temperature fluctuations (Fig. 2A-B). Earlier observations with a Simrad SM2000 in July 2000 suggested even higher backscattering corresponding only to the predictions of temperature fluctuations (Fig. 2B). In related field measurements applying the acoustic scintillation technique to a hydrothermal plume above a neighboring mound of Grotto, Xu and Di Iorio (2012) found that the forward-scattered signals are dominated by the temperature fluctuations within the plume. They also estimated the volume backscattering strength from the plume at 20 m above the mound to be $10\log_{10}(\sigma_b/1\text{m}^{-1}) \sim -70$ dB based on the sound scattering properties obtained by inverting the forward scattering data. While the COVIS scan here has slightly higher scattering in the plume (-60 to -80 dB in Fig. 2A), this scan was taken much lower in the plume (6 m above the mound).

The results above corroborate the view that temperature fluctuations, as opposed to particles, are the dominant backscattering mechanism within a hydrothermal plume. As a result, a sonar image of a hydrothermal plume (as in the slice in Fig. 1A or the volumes in Figs. 3-7) can be viewed as a reflection of the turbulence in the temperature field within the plume. In many aspects (such as determining the expansion rate of a plume), the temperature fluctuation distribution is similar (but not identical) to the particle distribution as both behave somewhat like passive tracers. Thus, the calculations previously reported have validity, although their interpretation is somewhat changed.

3.0 Sonar engineering

Having established both a theoretical basis and a practical demonstration for the acoustic detection of hydrothermal plumes (section 2), the next step was to design a sonar system for acoustic imaging that could fulfil the potential promises of acoustic imaging (section 1.3). Practical acoustic imaging of hydrothermal plumes depends on two elements: (1) modifications of an appropriate commercial sonar to record the time-varying sonar signal (rather than just the first return used by bathymetric mapping); and (2) mounting said sonar on 1 or more rotational axes driven by motors. The rotational mount is critical to obtaining three dimensions; while one dimension comes from the time-distance relationship of the acoustic signal, the others come from rotation or multiple receiver beams. The first acoustic images of hydrothermal plumes were obtained using a Mesotech 971 (330 kHz; 100 µm pulse) modified with a conical (1.7°) beam and two rotational motors to sweep out a 3D volume (Fig. 1B; Rona et al., 1991). Later applications used multibeam sonars (Simrad SM2000 and Reson Seabat 7125) reducing the need to only a single rotational motor for full 3D coverage (Fig. 1C-D). Although full 3D multibeams have been considered, they are not at present practical given the weight and size requirements for use on underwater vehicles. Table 2 compares four different sonar setups used for acoustic imaging of hydrothermal plumes.

The initial sonar setup in 1990 recorded only the magnitude of the pressure wave (in volts). This proved inadequate for quantitative analysis in part because the spectral content of the signal is lost. The sonar backscatter signal is digitized and digitally basebanded to reduce the size of the data stream. The baseband signal is a complex-valued representation of the real-valued modulated physical backscatter signal and is referred to as the complex waveform. Recording the complex waveform enabled analysis for the Doppler shift (Jackson et al., 2003) and the use of ping-to-ping correspondence in identifying the turbulent features (Rona et al., 1997). The Mesotech 971 was modified to record the complex waveform for the 1996 data collection, and all subsequent sonars have been so modified (note that off-the-shelf sonars are rarely set to record the complex waveform). Additional modifications to record the outgoing signal facilitate the Doppler analysis.

While the initial 1984 test using an opportunistic sonar showed that a 37 kHz frequency can be used to detect hydrothermal plumes, all subsequent tests have chosen to use higher frequency sonars ranging from 200 kHz to 400 kHz, as these higher frequencies give better resolution of ping-to-ping phase change and Doppler shift. Pulse lengths have generally been set according to the intended application as shorter pulses give better imaging resolution (useful for both diffuse mapping and plume imaging), but longer pulses provide better Doppler resolution.

Additional engineering changes were driven by the differing needs of working with a remote operated vehicle (ROV) compared to a submersible and later by the yet different needs of installation and use on a cabled observatory. Thus, the final (COVIS) setup has more (3) axes of rotation than the earlier Mesotech (2 axes) or Simrad (1 axis) setups to allow for re-leveling of the sonar head at need (i.e., after initial installation and anytime, accidental or deliberate, the platform is moved) (Fig. 1C). This has been critical in maintaining long-term (four years) operations despite accidental minor entanglement of the platform with a ROV cable in 2013.

3.1 initial results

The first test of the Mesotech-submersible acoustic imaging system was conducted at the Southwest vent field, at 21°N and a depth of 2635 m on the East Pacific Rise (EPR) because of the favorable seafloor geometry (isolated vents in open terrain), the likelihood of a low sea surface (good weather in November 1990), and relatively easy logistics. The chosen target consisted of two adjacent black smokers discharging from chimneys situated on the edge of a field of pillow lavas called Clam

Acres. The 1990 cruise collected at least 4 individual acoustic images (3D volume data), a short series of sectors at different elevations, and a longer series at a single point. A single acoustic image from the 1990 cruise spectacularly illustrates the various components of hydrothermal discharge, including patchy diffuse flow around the base of the chimneys, the chimneys themselves, two separate buoyant plumes, coalescing plumes, and bending plumes (Fig. 3; Rona et al., 1991). The time series of the single beam held stationary showed the variation in backscattering intensity over short time scales (seconds to minutes) relevant to eddy dynamics establishing the potential for monitoring hydrothermal plumes.

4 Methods of processing for flow characteristics

Straight-forward reconstruction of the 3D acoustic images produces vivid and visually attractive images, but does not yield quantitative results. To do actual science, we need to learn how to extract the regions of interest (i.e., the plume(s)) from the background data in order to estimate the specific information needed for scientific understanding of plume behavior and hydrothermal fluxes; such extraction is an ongoing focus of visualization research (e.g., Silver and Zabusky, 1993; Silver and Wang, 1996; Rona et al., 1998; Ozer et al., 2014). Starting in the 1990's, various projects have investigated a series of techniques for portraying different aspects of hydrothermal plumes, developed methods to extract quantitative properties (such as centerlines and rates of expansion), and explored alternative ways to use a sonar to detect hydrothermal discharge. By the early 2000's, each beautifully visualized sonar image was accompanied by a data set indicating the presence and structure of a centerline, the rates of expansion of the plume edges and estimates of dilution rates (Rona et al., 2002). We'd learned that multiple black smokers often combined to make one larger plume and that studying the dynamics of such plumes demands a variety of new measurements (Bemis et al., 2002).

Over the last two decades, joint development of visualization and acoustic methods has supported the scientific investigation and monitoring of hydrothermal plumes and other flow regimes (Table 1). Currently, there are three distinct modes of sonar use for estimating hydrothermal flow characteristics: (1) from the beginning in the late 1980's/early 1990's, the sonar was used in a classical imaging mode to determine the boundaries of the plumes rising from hydrothermal vents; (2) an alternative processing of complex waveform data estimates the Doppler shift, and from it velocities, as an alternative Doppler mode of sonar use; (3) an alternative sonar transmit head and data processing have also been developed for mapping the extent of diffuse flow; this is termed the diffuse mode of sonar use. The methods of visualization, quantification, and detection presented in this section (sections 4.0-4.1) largely apply to the use of the sonar for imaging in 3D. Some (like the geometric reconstruction) also apply to the Doppler mode. Separate sub-sections will cover the specifics of the Doppler (section 4.3) and diffuse (section 4.2) modes. Table 3 presents an overview of processing steps (acoustic and visualization) discussed in sections 4.1-4.

4.1 Methods for quantification and visualization of sonar images

The raw acoustic data is organized in pings at specified azimuths and elevations with the earlier (conical beam) data coming as a single azimuth (and elevation) per ping (or burst of pings) and the later (multi-beam) data as a single elevation (at all azimuths) per ping (or burst of pings). Beamforming resolves the multi-channel signals into directional beams (each channel corresponding to a single receiver element in the multi-beam sonar). Range from the sonar is based on the two-way travel time for each ping to travel out, be backscattered, and return. The 3D volume is reconstructed by effectively stacking the horizontal scans, although in actual computations the values at points in a uniform grid are distance-

weighted averages of the nearest points in the structured coordinate system of azimuth, elevation, and time-distance (Rona et al., 2002).

Time-varying gain, filtering, and calibrations ensure that the signal is reported as volume backscattering cross-section (units of 1/m). Many sonars standardly correct for spherical spreading using a time-varying gain that is applied within the sonar head (which contains a full CPU) before recording the signal; this was used in the Simrad but disabled in the Reson. In all cases, range-dependent corrections are applied in processing to fully account for spherical spreading and other distance dependent effects. For the earlier sonars, filtering was largely applied during data processing; COVIS's Reson sonar applies some filtering before the signal is recorded. The Mesotech data in both 1990 and 1996 consisted of only one ping per azimuth, but traversal across the azimuths and elevations takes several minutes; thus, the Mesotech images can be considered somewhat asynchronous snapshots (Bemis et al., 2002). The Simrad data have one or two pings per elevation; when pings are paired, they are processed pairwise as either complex sums or differences. The results of each pair or single ping are placed into a uniform spatial grid with trilinear interpolation. As the range of elevations is traversed multiple times, the results can be averaged. The COVIS imaging data are in bursts of approximately 6 pings at each elevation, which are processed pairwise as either complex sums or differences and then averaged over the pairs, providing a similar level of averaging. The SM2000 and COVIS acoustic images are more analogous to time-lapse photos than to snapshots.

The complex differences of paired scans mentioned in the previous paragraph enhances signals scattered by moving or turbulent features (which result in variable phase shifts) over scattering from stationary objects (which should scatter at a constant phase); thus, out-of-plane (sidelobe) returns from the seafloor and sulfide structures are suppressed (Fig. 4B). A corrective factor of 0.5 is applied to the magnitude of the differences before averaging to keep the intensity levels similar to those of a single ping (compare the isosurfaces in Figs. 4A and 4B which are set at the same levels). Data files are prepared for archive store double grids (one of differences and one of the more standard sums) to ensure immediate availability of interpretable intensity values as well as corrected images.

Once the backscattering cross-section, or intensity, has been gridded, the next steps are to visualize the data and to extract useful properties. From the beginning, layered partially-transparent isosurfaces have been the standby method of visualizing acoustic images of plumes (e.g., Rona et al., 1991). However, other visualization tools have been explored including ray-tracing and related volume renderings (Fig. 5; Santilli et al., 2004).

Extracting quantitative properties first requires isolating the plume (or plumes) from the background. In the visualization literature, this is variably referred to as segmentation and/or extraction. Each node or element of the grid (termed a volume element or voxel) is labeled as plume or background; this can be accomplished by simple thresholding, but the thresholding process alone does not yield any information on connectivity (Fig. 6A).

Features (like a plume) are isolated from the background region (less than threshold) by applying three dimensional region-growing algorithms to the gridded data (Silver and Zabusky, 1993; Silver and Wang, 1996). The region-growing algorithm applied in this work iteratively scans each voxel of data, and chooses an unvisited voxel with intensity greater than the predefined threshold as a seed point. Each seed point is assigned a unique feature ID. The algorithm continues to recursively search all adjacent voxels of the chosen seed point, and those with intensity greater than the threshold are labeled as belonging to the current feature. All searched voxels are marked as visited. The current feature stops growing when only voxels with values less than the threshold are encountered in all growing directions.

The set of voxels that constitute the feature are stored in a data structure for efficient manipulation (Silver and Wang, 1996). The region growing process is completed when all voxels in the data are visited.

Regardless of the segmentation method, the outer surface of the plume object will be an isosurface determined by the specified threshold. Global properties (often termed attributes), such as volume, local maximum, and moments of inertia, can be calculated for each resulting object (Rona et al., 2002). Furthermore, pre-specified shapes can be fit to the objects to clarify aspects of the surface irregularities. For plume, this means that the indentations and crenulation indicative of eddies, spiraling, and related entrainment processes can be visualized and measured (Fig. 3C; Rona et al., 1998; Bemis et al., 2000; Rona et al., 2002).

Because fluid dynamic descriptions of hydrothermal plumes generally references all properties to height above the vent and to distance from the core of the plume (e.g., Morton et al., 1956), further quantification requires the determination of a practical centerline. In early (and some current) applications, centerlines were defined using a series of horizontal slices at varying heights above the vent (Bemis et al., 2000). The actual center on each slice was defined as a center of maxima (which looked for local or global maxima), a center of mass (which considered the distribution of intensity) or a center of volume (which is based on the edge of the thresholded region). Applying this to the Clam Acres plumes suggested that the center of mass or local maxima is the most indicative attribute of the fluid flow behavior (Fig. 6B-C; Rona et al., 1998, 2002). Combining starting seed point near the vent and tracking local maxima or centers of mass vertically proved particularly useful in detecting the merging of the two Clam Acres plumes (Rona et al., 1998, 2002).

Using slices perpendicular to the plume at multiple heights, a variety of properties relevant to the fluid mechanics can be estimated, including the centerline intensity and the radius of the isosurface (Rona et al., 2002). The radius is dependent on the threshold chosen in the segmentation step. Combining the radii from several thresholds provided a 2D glimpse of the intensity distribution within the plume and a crude estimate of the plume e-folding radius and expansion with height (Fig. 6E; Rona et al., 2002). Comparisons of the centerline tracks, the isosurface and plume radii, and dilution behavior for different plumes lead to a deeper understanding of the dynamics of hydrothermal plumes. Bemis et al. (2002) demonstrated that the presence of multiple sources (black smokers) in a small region can result in a merged plume that narrows (and presumably rises faster) before expanding due to entrainment of ambient seawater (Fig. 7).

Several advances have been made in centerline and plume property computations. Skeletons can be determined for the plume objects using applications of field potential theory (Gagvani and Silver, 1999; Wan et al., 2001; Sundar et al., 2003; Cornea et al., 2005; Cornea et al., 2007). A centerline computed by such a distance matrix-based curve-skeleton algorithm can be used to accurately estimate the direction and degree of bending of the plume using least squares analysis. More accurate estimates of plume properties as a function of height can be obtained by fitting a Gaussian (or other appropriate distribution) to the slice-wise distributions (Rona et al., 2006). These properties include the peak intensity (based on the overall distribution rather than local maxima), the peak location, and the e-folding radius of the plume.

Additional explorations of internal eddy structure have considered the differences between individual volumes of data and the average of several such volumes (Fig. 8), the eddy-like features visible on isosurfaces (Figs. 3-6) and within volumes (Fig. 8A) and the ratio between surface area to volume as a function of grid spacing and isosurface value. With more averaging available, the internal plume structure is simpler and the plume edges better defined; this corresponds well with classical

plume theories which are all based on time averaged properties (Fig. 8B; Rona et al., 2002). Without averaging, the larger scales of the internal eddy structure can be discerned. The 0.25-1.0 m resolution of the acoustic data prevents the smallest scales from being resolved (Fig. 8A).

4.2 Detecting diffuse flow

Hydrothermal discharge occurs in multiple forms: the black smoker generated plumes are the most visually prominent, but the low temperature more subtle diffuse flow may transport as much or more heat (e.g., Rona and Trivett, 1992; Viers et al., 2006; Rona et al., 2015). Diffuse discharge may be visible as a shimmering in the water above the site of discharge or covered by lush biomass which obscures the fluid flow (Bemis et al., 2012). Thus, detailed mapping based on video, even when available, would reflect the distribution of biomass more than the distribution of discharge. Rona et al. (1997) initiated an exploration of alternative acoustic methods for estimating the area of discharge.

Diffuse flow typically is lower in particle content (appearing clear) as well as temperature, but still highly turbulent. The turbulent fluctuations in temperature that produce the visible shimmering can also shift the phase of acoustic signals transmitted through the diffuse flow discharge (Jackson and Dworski, 1992; Rona and Jones, 2009). Because significant decorrelation occurs for even fairly small temperature fluctuations ($dT < 1^\circ\text{C}$), the decorrelation estimate is an effective detector of low temperature turbulent fluids such as hydrothermal diffuse discharge (Jackson and Dworski, 1992).

With the later sonars (Mesotech reconfigured, Simrad and Reson), the configuration allowed the complex waveform to be recorded. Combining the recording of the complex waveform with the use of a wide angle (20°) transducer (instead of the usual narrow beam transducer) permitted the capture of decorrelation signatures over a broad area. Multiple scans with different headings or elevations are combined to further increase coverage (Fig. 9; Rona et al., 1997, 2015; Rona and Jones, 2009)). The first application compared a composite of 17 sector (60°) scans with the same heading but varying elevations covering a 30 m deep range with mapped diffuse flow features (Rona et al., 1997). Several applications using the Simrad setup explored acquiring spatial coverage by changing the heading between scans (Fig. 9).

The geometric reconstruction for the diffuse mode is similar to that for the imaging mode except that the 3D locations are projected onto a 2D grid based on the intersection of seafloor and ping for a given elevation and the broadening of the elevation range for a given ping due to the wide angle transducer. Multiple pings are collected for each elevation. For each pair of pings at a given location, two quantities are estimated: the amount of phase shift or decorrelation between pings and the strength of the backscattering signal. The decorrelation results and the backscatter intensity are independently averaged over a short series of pings (for the Mesotech in 1997, 5 pings spaced at 142.9 s intervals; for the Simrad in 2000, 2 or more pings at 0.1 s intervals; for COVIS's Reson, ~10 pings at 0.25 s intervals). Sensor motion, noise and perhaps ambient ocean turbulence will also cause signal decorrelation. For the Mesotech and Simrad, a correction for the effects of low signal-to-noise levels, when the return from the seafloor is weak, was made by using the product of the decorrelation and the backscatter intensity rather than the pure decorrelation. With COVIS, an alternative approach of thresholding on the backscatter intensity to select areas with sufficient signal-to-noise ratios was used and the pure decorrelation reported within those areas; the advantage is more interpretable units (Rona et al., 2015). Repeated mapping of the same areas by COVIS suggests that the area extent of diffuse flow may vary greatly over tidal and longer periods (Rona et al., 2015).

4.3 Estimating vertical flow

Recording the complex waveform also enabled the estimation of incoherent Doppler shifts. Jackson et al. (2003) used the 2000 data from the Simrad SM2000 to explore the use of Doppler frequency shifts to estimate line-of-sight velocities. The recognition that the bending of the plume centerline provides an estimate of horizontal flow relative to the average rise rate in the plume meant we could finally estimate vertical velocity (Jackson et al., 2003), and estimates of vertical velocity lead to estimates of volume flux and heat flux.

Using the Simrad sonar in 2000, the Doppler mode consisted of bursts at each elevation of 10 pings (as a 1.2 ms pulse) separated by 0.2s and stepping through the elevations from roughly horizontal to nearly vertical in 1° steps (Jackson et al., 2003). With COVIS, the number of pings per burst was increased to 40 and the length of the pulse to 1.5 ms to improve the signal-to-noise ratio. COVIS's elevation range starts at 20° above horizontal as COVIS sits well below the vents (Xu et al., 2013).

The analysis of the Doppler frequency shift observed in the volume backscattering strength σ_b using a covariance method yields the plume velocity component along the acoustic line-of-sight (V_r) (Jackson et al., 2003). Both volume backscattering strength σ_b and the acoustic line-of-sight velocity V_r are obtained before gridding. The gridding proceeds as described in section 4.1 for the imaging mode except that the Doppler mode uses more pings per elevation.

After gridding, a geometric conversion of the gridded line-of-sight V_r data estimates the vertical velocity component W of the plume (Fig. 10; Jackson et al., 2003; Xu et al., 2013). Further analysis of volume backscattering strength σ_b and vertical velocity W yields key plume physical properties, including plume radius, volume flux, and expansion rate (Rona et al., 2002; Xu et al., 2013). Subsequently, the initial buoyancy flux and hence the heat flux of the plume can be estimated based on the classic formula for a buoyancy driven plume (Xu et al., 2014).

4.4 Initial attempts at monitoring

The next step is monitoring to obtain a time series. Both the earlier series of frames from 1990 (Fig. 3) and a 24-hour time series collected in 2000 (Fig. 11) yielded brief glimpses of the ever-changing bending plumes and the influence of tidal forces on entrainment (Rona et al., 2006). Section 5.2 discusses some of these results.

5 Science learned

As acoustic data showing the overall behavior and internal structure of plumes accumulate, perceptions and understandings of plume dynamics shift. This section first summarizes the scientific results covered in sections 2-4 and then looks at some of the key insights garnered at different stages in the processes of developing the acoustic imaging technique for hydrothermal plumes.

Several major scientific findings arose from the early development of acoustic imaging of hydrothermal plumes. Quantitative analysis established that hydrothermal plumes are structured similar to laboratory and model plumes, with a centerline along which vertical velocity and backscattering strength decrease with height above the vent(s) and with more-or-less Gaussian profiles perpendicular to the centerline (section 4.1; Figs. 6-7, 11; Bemis et al., 2002; Rona et al., 2002). The plumes bend with periodicities similar to the semi-diurnal tidal cycle; the expansion and entrainment rates of the plume increase with bending (section 4.4; Fig. 11; see also section 5.2; Rona et al., 2006). Volume flux is estimated from the horizontal profiles of vertical velocity (section 4.3; Xu et al., 2013). The inversion of volume flux variation with height above the vents leads to estimates of heat flux for the plume source(s). Although short-term variance is quite high, the longer term volume and heat flux

seems stable (section 6; Fig. 14; Xu et al., 2014). Diffuse flow can be detected using acoustics and varies over time (Rona et al., 1997, 2015). Long-term monitoring has shown strong tidal-scale periodicities of plume bending and diffuse flow area (section 6; Fig. 14). Besides the tidal periodicity, plume bending also clearly indicates the asymmetry of local currents, suggesting a mean flow northwards in the rift valley and also giving indications of 4-6 day episodic excursions in direction that may relate to internal ocean waves (section 6).

5.1 Merging plumes

The interaction and merging of plumes due to mutual entrainment have been discussed theoretically in many contexts (e.g., Davidson et al., 1994; Kaye and Linden, 2004). Here we can use acoustic imaging to document the interaction of plumes discharging from nearby black smokers. The plumes interact through their entrainment fields and sometimes merge. Figs. 3, 5, and 6 show the merging of two plumes in a relatively simple setting in Clam Acres. Both the Monolith (1996 Mesotech data) and Grotto (2000 Simrad data and 2010+ COVIS data) vents have multiple black smokers in close proximity (<5 m separation), and the resulting plumes show one or more predictable effects of merging (i.e., necking isosurfaces, velocity increases at merging level, and asymptotic equivalence to a single stronger vent post merging) (see Fig. 7 for Monolith; see Figs. 4, 8, or 11 for Grotto). Fig. 12 shows the results of an entrainment field-based model compared with velocity estimates from the Simrad data acquired in July 2000 at Grotto (Rona et al., 2003). As anticipated for a vent with at least 5 smokers feeding its plume (Rona et al., 2015), there is a substantial increase in velocity above the vents.

5.2 Tidally driven changes in bending and entrainment

Initial clues to the true depth of impact of tidal processes on hydrothermal plumes came with the 24 hour time series collected in 2000 which showed that not only did the plume bend back and forth with the tides (Fig. 10) but also the apparent entrainment varied (Rona et al., 2006). Highly bent plumes expand faster than vertical plumes. Rona et al. (2006) explained this as forced entrainment due to the tidal current impinging on the plume edge. Xu and Di Iorio (2012) provide a formulation relating the ambient current speed and the enhanced entrainment. They also used acoustic scintillation data to demonstrate that the cooling impact of such enhanced entrainment in reducing the buoyant rise rate. Later, COVIS data also showed reduced rise rates corresponding to enhanced plume expansion (Xu et al., 2013). Several modelling efforts confirm the effect of tidal cycles on plume bending, forced entrainment and plume expansion (Lavelle, 1997; Lavelle, et al., 2013).

6 Introducing COVIS

In their initial use of acoustic imaging to detect and describe hydrothermal plumes, Rona et al (1991) considered the potential for long-term (years to decades) monitoring of plumes using a sonar. The main limitations on long-term acoustic monitoring are the requirements for an ongoing power supply, a method of data retrieval to keep local hard-drives from overfilling, and a stable platform with a rotation system (Bemis et al., 2014). New technological developments such as underwater junction boxes, ROV (Remotely Operated Vehicle) underwater mateable fiber/copper connectors, and new fiber optics protocols have recently enabled long-term monitoring through cabled seafloor observatories such as The North East Pacific Time-series Underwater Networked Experiment (NEPTUNE) observatory (Favali et al., 2010). The NEPTUNE observatory supplies power (up to 10 kW), high data-bandwidths (up to 10 Gbs), and interactive access through standard internet protocols along its fiber optic cables. Its installation at the Endeavour Segment of the Juan de Fuca Ridge via Ocean Network Canada (<http://www.oceannetworks.ca>) enables scientists to study the response of a hydrothermal system to

geological events through continuous long-term, high temporal resolution observations using both acoustic and traditional sensors.

The Cabled Observatory Vent Imaging System (COVIS) was specifically designed to connect to the NEPTUNE Canada cabled ocean observatory with the goals of: (1) visualizing the behavior of the high temperature focused plume; (2) quantifying the outflow fluxes of the same; and (3) mapping low temperature diffuse hydrothermal discharge near the seafloor. The NEPTUNE ports provide 375VDC and 1 Gigabit Ethernet interface to the instrument through a submarine cable. COVIS is a 4-m tall titanium tripod on which the sonar (a modified Reson Seabat 7125) and cable observatory interface systems are mounted (Fig. 13). A unique 3-degrees of freedom (pitch, roll, yaw) mechanical rotation system allows for the sonar transducers to be aimed appropriately at the hydrothermal vent and mechanically scan the sonar across the vent plume. The rotation system allows a large range of pitch, roll, and yaw angles for observing any structures within the sonar range at the installation site.

The projector produces a 400kHz, 1 degree (vertical width) by 128° (horizontal width) fan beam with 256 receive beams of width 0.5° and spacing 0.5° when making measurements of the plume extent and during collection of data for Doppler processing for plume velocities. The sonar boresight is mechanically stepped in 1° increments to image the plume from the vent orifice to an upward angle of 60°. A different projector is used with a vertically much broader beam to make measurements of the diffuse flow around the base of the vent structures. This projector produces a 200 kHz, 30° (vertical width) by 128° (horizontal width) fan beam with 128 receive beams of 1° width and 1° spacing. A single elevation angle is used in this (the diffuse) case.

Metadata from rotation motor position sensors and a sonar-mounted attitude sensor (magnetic heading, gravity sensing pitch/roll) along with system health information is streamed during operation for real-time monitoring. Sonar data are stored locally on the platform with a modest capacity (several days). NEPTUNE Data Management and Archiving (DMAS) software periodically uploads the sonar data files making best use of network bandwidth and decoupling the real time sonar data acquisition. Sonar data are post-processed automatically upon delivery to shore with several plume image and Doppler data products available via the NC data management website (<http://oceannetworks.ca>).

6.1 Preliminary results from COVIS

In September 2010, COVIS was deployed at 47°57'N, 129°6'W, approximately 30 m to the northeast of the Grotto mound, a hydrothermal vent cluster on the Endeavour Segment of the Juan de Fuca Ridge in the Northeast Pacific, and connected to the NEPTUNE observatory (Fig. 13). COVIS sits between jumbled blocks of basalt looking up at the Grotto and Dante vent sites. This ability to minimize interference in the vent ecosystem while still quantitatively monitoring the hydrothermal discharge is an asset in the Endeavour Marine Protected Area.

An extended and ongoing sequence of 2D and 3D acoustic data has been collected by COVIS including 26 days after its installation in 2010 and a continuing time series since September 28, 2011. Fig. 4 shows an example of the imaging mode data from COVIS. Looking at a time series of scalar properties extractable from the imaging, Doppler and diffuse mode data (Fig. 14) strongly suggest a dominant periodicity. Spectral analysis confirms that this periodicity (~2cycles/day) is consistent with a tidally-driven system (see examples in Fig. 16). However, we observe several breaks in the periodicity, which indicate the influence of other processes. Also, the bending components are shifted N and E of symmetric suggesting a background flow to the northeast, probably along the rift valley. Initial results for time series of volume flux and heat flux are presented in Xu et al. (2013, 2014). Increasingly, correspondences (and lack thereof) in periodicity between data for different parts of Grotto and for

different aspects of the hydrothermal system suggest a common impact of tidal and subsurface factors across Grotto. Fig. 14 compares the plume bending and vertical velocity and diffuse areal extent measured by COVIS with the temperatures of both black smokers (measured by BARS) and diffuse flow (measured by RAS) to see a common periodicity.

6.2 New visualizations for COVIS

Given the extended time series available for COVIS (some thousands of time steps over four years of acquisition to date), we have explored alternative ways both to search for interesting events and to display the overall characteristics of those events (Liu et al., 2013; Ozer et al., 2014). The feature tracking framework (Silver and Wang 1996) has been applied on COVIS data to extract, track and quantify several properties of the plumes that exist in the COVIS data (see Figs. 15A-B). More recent visualization techniques include classifying time sequences based on user-defined models that consider what anomalous sequences of bending states might exist (Ozer et al. 2014). Liu et al. (2013) developed a graphical user interface (GUI) for the modeling, tracking, classifying, and visualizing. One interesting new visualization technique involves classifying each time step according to the degree of plume bending (Fig. 15) and then averaging those in a similar state. The repeat rates of the resulting classes clearly mimic a tidally-driven bending sequence (Fig. 16).

The application of feature tracking and the development of an average visualization was motivated by the question, “What does typical plume bending look like?” We observed that the currents driving plume bending normally push the plume in directions that vary in an elongated ellipse such that the primary motion appears as sloshing back-and-forth along the long axis of the ellipse (or, geologically, along the axis of the rift valley). The bending angles are least squares estimated from plume centerline or skeleton computed by a distance matrix-based curve-skeleton algorithm (Gagvani and Silver, 1999; Cornea et al, 2005). By defining each set of similar directions of plume bending as an object state, we assign five states (P1: extreme bending to south; P2: mild bending to south; P3: little to no bending; P4: mild bending to north; P5: extreme bending to north) to model the plume bending activity based on the azimuth or direction of bending and the amount of bending (Figs. 15 and 16). For the data in Fig. 16A-C, the skeletons, centerlines, and classification were computed only for the biggest plume in COVIS’s acoustic images acquired during October 2010. The set of plume time steps in each state is averaged to create a “key” frame sequence describing the typical bending event in current state (Fig. 16C). This is similar to “illustrative” visualization where a scientist may draw a picture depicting different steps in an activity.

The resulting set of images (Fig. 16C) shows a clear asymmetry in the bending directions: the plume bends much more strongly to the north than to the south. This is consistent with other observations of a mean northward flow in parts of the Endeavour Segment rift valley (e.g., Thomson et al., 2009). Additionally, although the timeline of bending incidences (Fig. 16A) looks erratic, spectral analyses of these timelines confirm that the respective bending positions are repeated twice daily (Fig. 16B). The event detection and related visualizations provide a means to confirm and illustrate the behavior inherent in spectral analyses of the overall plume bending data set. Eventually, such a visometric approach will provide the basis for understanding the episodic excursions away from the normal periodicity.

7 Discussion and Conclusions

Acoustic imaging (and related Doppler processing) has demonstrated the potential to overcome many of the limitations of standard short-term spot measurements. Mounting a multi-beam sonar on a platform capable of at least one direction of rotation enables fully three-dimensional imaging and reduces the lack of simultaneity of the resulting data set (Rona et al., 2002). Quantitative estimates of heat flux, volume flux, vertical velocity, plume orientation, and entrainment rates have been obtained for selected sites (e.g., Rona et al., 2006; Xu et al., 2014). Finally, attaching such a sonar system to a cabled observatory enables long-term monitoring to see how the plumes and other hydrothermal discharge vary in time (Rona and Light, 2011).

By and large, the original objectives (section 1.3) mentioned in Palmer et al (1986) have been achieved. Acoustic imaging readily detects the extent of the plume and provides direct estimates of the expansion and entrainment rates. Due to limitations on the distances at which the plume can be acoustically imaged (<100 m using 200-400 kHz), incursions as a neutrally buoyant layer are better captured using CTDs on deep tows or autonomous vehicles, although the height of the neutrally buoyant layer can be inferred from the acoustic-based estimates of heat flux. Doppler shifts captured acoustically yield accurate estimates of the vertical rise rates, volume fluxes and heat fluxes for hydrothermal plumes. However, the estimation of particle concentrations has proved infeasible as the main scattering mechanism has proven to be temperature fluctuations rather than particulates based on previous observations of particle sizes and on the observed volume backscattering strength. Little effort has been made to see if the distribution of backscattering intensity can be used to estimate temperature distributions instead of the predicted particle distributions. This is a potential area for future research. The ability to use acoustic imaging to map the extent of diffuse flow, and potentially its intensity, is an unanticipated but fruitful development.

COVIS's observations of plume bending and volume flux highlight the potential for long-term monitoring via remote sensing in this Marine Protected Area. Recent studies have led to the inversion of volume flux observations for heat flux in the discharging plumes, which provides a key constraint for modelling magmatic-hydrothermal processes beneath the vent field. Efforts to identify geologic events have led to the recognition of the transient effects of atmospheric storms on plume behavior. Investigations into the potential correlations between plume variability and local earthquakes are ongoing. Most of the existing work has focused on the strong plume above Grotto's North Tower but there are two additional plumes visible in the acoustic images (Figs. 3-7). This is another potential area for future research.

The development of acoustic imaging as a technique for measuring plume properties and of COVIS as a practical platform opens many doors. Future work with a cabled observatory platform like COVIS could include further ground-truthing, especially of the diffuse flow mapping capabilities, imaging of other nearby plumes, such as Dante, and the duplication of COVIS elsewhere. Much potential still rests in the use of acoustic imaging from submersible, ROV or AUV platforms although not all of the quantifications are possible on a moving platform.

Acknowledgements

The development of acoustic imaging for hydrothermal plumes would not have been possible without the leadership and contributions of Peter Rona. This paper is a tribute to his unwavering pursuit of science. Thanks to all who have worked with COVIS or the acoustic imaging team. In addition to the named authors, we would like to thank our colleagues in acoustics (esp., Dave Palmer), engineering (esp., Vern Miller, Mike Kenny and Tim Wen), visualization (esp., Jay Takle, Jamshed Dastur, Dilip

Hosehote-Kenchamena, Simon Wang, Nicu Cornea, Jeff Rabinowitz, Kristina Bennet, Peter Lin, Min Chen, Simon Walton, Alfie Abdul-Rauman), and oceanography-geology (Keven Hart, Christine Jedrzejczyk, Kyohiko Mitsuza, Dave Butterfield, Marv Lilley, Bob Embley, Mike Carr, Mike Kennish and Rich Lutz) for participation in various cruises, fruitful discussions, and assistance. We thank the many funding agencies who have supported our work in acoustic imaging: NSF OCE (1234141, 1234163, 9818841, 9911523), OTIC (0824612, 0825088) & CISE (0312272, 070247), NOAA NURP and otherwise, NRL, NEPTUNE, GSA. We thank the ship, submersible and vehicle crews including those of the R/V Laney Chauest, R/V Thompson, ROV Jason, Navy ATV, DSV Turtle, DSV SeaCliff, CSSF Tully, and ROV ROPOS. We thank the staff and scientists of Ocean Networks Canada for their ongoing support of COVIS on the NEPTUNE observatory (esp., Maia Hoebrechts, Steve Mihaly, Renya Jenkins, Ben Biffard, Dwight Owens, Benoit Pirene, and Kim Juniper).

References

- Baker, E. T., 2007. Hydrothermal cooling of midocean ridge axes: Do measured and modeled heat fluxes agree?, *Earth and Planet. Sci. Letters* 263(1), 140-150.
- Baker, E. T., Massoth, G.T., 1987. Characteristics of hydrothermal plumes from two vent fields on the Juan de Fuca Ridge, northeast Pacific Ocean. *Earth Planet. Sci. Lett.* 85, 59-73.
- Barreyre, T., Escartin, J., Garcia, R., Cannat, M., Mittelstaedt, E., Prados, R., 2012. Structure, temporal evolution, and heat flux estimates from the Lucky Strike deep-sea hydrothermal field derived from seafloor image mosaics. *Geochemistry, Geophysics, Geosystems* 13(4), 10.1029/2011GC003990.
- Bates, A.E., Lee, R.W., Tunnicliffe, V., Lamare, M.D., 2010. Deep-sea hydrothermal vent animals seek cool fluids in a highly variable thermal environment. *Nature Commun.* 1, 1–6, doi:10.1038/ncomms1014.
- Bemis, K. G., R.P.V. Herzen, R.P.V., Mottl, M. J., 1993. Geothermal heat flux from hydrothermal plumes on the Juan de Fuca Ridge, *J. Geophys. Res.* 98, 6351–6365.
- Bemis, K., Lowell, R., Farough, A., 2012. Diffuse flow on and around hydrothermal vents at mid-ocean ridges, *Oceanography* 25(1), 182-191, <http://dx.doi.org/10.5670/oceanog.2012.16>.
- Bemis, K.G., Rona, P.A., Jackson, D., Jones, C., Silver, D., Mitsuza, K., 2002. A comparison of black smoker hydrothermal plume behavior at Monolith Vent and at Clam Acres vent field: dependence on source configuration, *Marine Geophys. Res.* 23, 81-96.
- Bemis, K., D. Silver, P. Rona, and J. Cowen, A particle sedimentation model of buoyant jets: observations of hydrothermal plumes, *Cahiers de Biologie Marine*, 47, 379-384. 2006
- Bemis, K. G., Silver, D., Rona, P., Feng, C., 2000. Case study: a methodology for plume visualization with application to real-time acquisition and navigation, In *Visualization 2000 Proceedings*, pp. 481-484. IEEE.
- Bemis, K. G., Xu, G., Jackson, D., Rona, P., Light, R., 2014. Cabled observatory enabled acoustic monitoring of hydrothermal discharge, UA2014, the 2nd international conference and exhibition on Underwater Acoustic, June 22-27.
- Bickle, M., Elderfield, H., 2004. Hydrothermal fluxes in a global context, In *Hydrogeology of the Ocean Lithosphere*, edited by E. Davis and H. Elderfield, Cambridge University Press, Cambridge, 677-690.
- Clague, D.A., Caress, D.W., Thomas, H., Thompson, D., Calarco, M., Holden, J., Butterfield, D., 2008. Abundance and distribution of hydrothermal chimneys and mounds on the Endeavour Ridge determined by 1-m resolution AUV multibeam mapping surveys. *Eos, Transactions, American Geophysical Union* 89(53): Fall Meeting Supplement Abstract V41B-2079.

- Converse, D. R., Holland, H.D., Edmond, J.M., 1984. Flow rates in the axial hot springs of the East Pacific Rise (21° N): Implications for the heat budget and formation of massive sulfide deposits, *Earth Planet. Sci. Lett.* 69, 159-175.
- Corliss, J. B., Dymond, J., Gordon, L. I., Edmond, J. M., von Herzen, R. P., Ballard, R. D., Green, K., Williams, D., Bainbridge, A., Crane, K., van Andel, T. H., 1979. Submarine Thermal Springs on the Galápagos Rift. *Science* 203, 1073-1083.
- Cornea, N. D., Silver, D., Min, P., 2005. Curve-skeleton applications, *Visualization, 2005, VIS 05. IEEE*. IEEE.
- Cornea, N., Silver, D., Patrick, M., 2007. Curve-skeleton properties, applications, and algorithms. *IEEE Transactions on Visualization and Computer Graphics* 13.3, 530-548.
- Crone, T. J., McDuff, R. E., Wilcock, W. S., 2008. Optical plume velocimetry: A new flow measurement technique for use in seafloor hydrothermal systems. *Experiments in Fluids* 45(5), 899-915.
- Davidson, M. J., Papps, D. A., Wood, I. R., 1994. The behaviour of merging buoyant jets. In Davies, P.A., Valente Neves, M. J. (Eds). *Recent research advances in the fluid mechanics of turbulent jets and plume*, NATO Advanced Research Workshop on Recent Research. Series E: Applied Sciences, Vol. 255, Kluwer Academic Publishers (Springer), Dordrecht, 465-478.
- Duda, T. F., Trivett, D. A., 1998. Predicted scattering of sound by diffuse hydrothermal vent plumes at mid-ocean ridges. *The Journal of the Acoustical Society of America* 103(1), 330-335.
- Favali, P., Person, R., Barnes, C.R., Kaneda, Y., Delaney, J.R., Hsu, S.K., 2010. Seafloor observatory science, In Hall, J. , Harrison, D.E., Stammer, D., (Eds.), *Proceedings of the OceanObs'09: Sustained Ocean. Observations and Information for Society conference 2*, Venice, Italy, 21-25 September 2009, ESA Publication WPP-306, 21-25
- Feely, R. A., Massoth, G. J., Trefry, J. H., Baker, E. T., Paulson, A. J., Lebon, G. T., 1994. Composition and sedimentation of hydrothermal plume particles from North Cleft segment, Juan de Fuca Ridge. *Journal of Geophysical Research: Solid Earth (1978–2012)* 99(B3), 4985-5006.
- Gagvani, N., Silver, D., 1999. Parameter-controlled volume thinning. *Graphical Models and Image Processing* 61.3, 149-164.
- German, C. R., Von Damm, K.L., 2006. Hydrothermal processes, In Elderfield, H., Holland, H., and Turekian, K., (Eds). *The Oceans and Marine Geochemistry(treatise on geochemistry series, volume 6)* , Elsevier, Oxford, 181-222.
- Govenar, B. , 2012. Energy transfer through food webs at hydrothermal vents: Linking the lithosphere to the biosphere. *Oceanography* 25(1), 246-255, <http://dx.doi.org/10.5670/oceanog.2012.23>.
- Hay, A. E., 1984. Remote acoustic imaging of the plume from a submarine spring in an arctic fjord. *Science* 225(4667), 1154-1156.
- Jackson, D.R., Jones,C.D., Rona, P.A., Bemis, K.G., 2003. A method for Doppler acoustic measurement of black smoker flow fields, *G³* 4(11), 1095, 1-12.
- Jackson, D. R., Dworski, J.G. , 1992. An acoustic backscatter thermometer for remotely mapping seafloor water temperature. *Journal of Geophysical Research: Oceans (1978–2012)* 97(C1), 761-767.
- Jaffe, J.S. 1990. Computer modeling and the design of optimal underwater imaging systems. *Oceanic Engineering, Journal of IEEE*, vol.15, no.2, pp.101,111..
- Kaye, N. B., Linden, P.F., 2004. Coalescing axisymmetric turbulent plumes. *Journal of Fluid Mechanics* 502, 41-63.
- Kocak, D.M., Fraser, R., Dalgleish, F., Caimi, M., Schechner, Y.Y., 2008. A focus on recent developments and trends in underwater imaging. *Marine Technology Society Journal* 42, no. 1, 52-67.
- Kwasnitschka, T., Hansteen, T. H., Devey, C. W., Kutterolf, S., 2013. Doing fieldwork on the seafloor: Photogrammetric techniques to yield 3D visual models from ROV video. *Computers & Geosciences* 52, 218-226.

- Lavelle, J.W., 1997. Buoyancy-driven plumes in rotating, stratified cross flows: Plume dependence on rotation, turbulent mixing, and cross-flow strength. *Journal of Geophysical Research: Oceans (1978–2012)* 102(C2), 3405-3420.
- Lavelle, J.W., Di Iorio, D., Rona, P., 2013. A turbulent convection model with an observational context for a deep-sea hydrothermal plume in a time-variable cross flow. *J. Geophys. Res. Oceans* 118, doi:10.1002/2013JC009165.
- Liu, L., Ozer, S., Bemis, K., Takle, J., Silver, D., 2013. An interactive method for activity detection visualization. *IEEE Symposium on Large Data Analysis and Visualization (LDAV)*.
- Little, S.A., Stolzenbach, K.D., Von Herzen, R.P., 1987. Measurements of plume flow from a hydrothermal vent field. *Journal of Geophysical Research: Solid Earth (1978–2012)* 92(B3), 2587-2596.
- Medwin, H., Clay, C.S., 1997. *Fundamentals of acoustical oceanography*. Academic Press, San Diego, 712 pages.
- Merewether, R., Olsson, M. S., Lonsdale, P., 1985. Acoustically detected hydrocarbon plumes rising from 2-km depths in Guaymas Basin, Gulf of California. *Journal of Geophysical Research: Solid Earth (1978–2012)* 90(B4), 3075-3085.
- Mittelstaedt, E., Escartín, J., Gracias, N., Olive, J. A., Barreyre, T., Davaille, A., Cannet, M., and Garcia, R., 2012. Quantifying diffuse and discrete venting at the Tour Eiffel vent site, Lucky Strike hydrothermal field. *Geochemistry, Geophysics, Geosystems*, 13(4), 10.1029/2011GC003991.
- Morton, B.R., Taylor, G., Turner, J.S., 1956. Turbulent gravitational convection from maintained and instantaneous sources. *Proceedings of the Royal Society of London. Series A. Mathematical and Physical Sciences* 234(1196), 1-23.
- Mottl, M.J., McConachy, T.F., 1990. Chemical processes in buoyant hydrothermal plumes on the East Pacific Rise near 21 N. *Geochimica et Cosmochimica Acta* 54(7), 1911-1927.
- Oeschger, J., Goodman, L., 1996. Acoustic scattering from a thermally driven buoyant plume. *The Journal of the Acoustical Society of America* 100(3), 1451-1462.
- Orr, M. H., Hess, F.R., 1978. Remote acoustic monitoring of natural suspensate distributions, active suspensate resuspension, and slope/shelf water intrusions. *Journal of Geophysical Research: Oceans (1978–2012)* 83(C8), 4062-4068.
- Ozer, S., Silver, D., Martin, P., Bemis, K., 2014. Activity Detection for Scientific Visualization, *IEEE Transactions in Visualization and Computer Graphics*, PP(99), doi 10.1109/TVCG.2013.117.
- Palmer, D.R., Rona, P.A., 2005. Acoustical imaging of deep ocean hydrothermal flows, in, H. Medwin and J.E. Blue, Editors, *Sounds in the Sea: from Ocean Acoustics to Acoustical Oceanography*, Cambridge University Press,Cambridge, 551-563.
- Palmer, D.R., Rona, P.A., Mottl, M.J., 1986. Acoustic imaging of high-temperature hydrothermal plumes at seafloor spreading centers, *J. Acoust. Soc. Amer* 80, 888-898.
- Ramondenc, P., Germanovich, L.N., Von Damm, K.L., Lowell, R.P., 2006. The first measurements of hydrothermal heat output at 9 50' N, East Pacific Rise. *Earth and Planetary Science Letters* 245(3), 487-497.
- Rona, P.A., Bemis, K.G., Jones, C.D., Jackson, D.R., Mitsuzawa, K., Silver, D., 2006. Entrainment and bending in a major hydrothermal plume, Main Endeavour Field, Juan de Fuca Ridge, *Geophysical Research Letters* 33, L19313, doi:10.1029/2006GL027211.
- Rona, P.A., Bemis, K.G., Silver, D., Jones, C.D., 2002. Acoustic imaging, visualization, and quantification of buoyant hydrothermal plumes in the ocean, *Marine Geophys. Res.* 23, 147-168, 2002.
- Rona, P., Bemis, K., Xu, G., Mitsuzawa, K., 2015. (this volume). Estimations of heat transfer from Grotto's North Tower: a NEPTUNE Observatory case study, submitted to DSRII Rona Special Issue, 2014.
- Rona, P., Bemis, K., Kenchammana-Hosekote, D., Silver, D., 1998. Acoustic imaging and visualization of plumes discharging from black smoker vents on the deep seafloor. In *Visualization'98, Proceedings* (pp. 475-478). IEEE.

- Rona, P.A., Light, R., 2011. Sonar images hydrothermal vents in seafloor observatory, *Eos*, 92(20), 17 May 2011, 169-170.
- Rona, P.A., Jackson, D.R., Wen, T., Jones, C., Mitsuzawa, K., Bemis, K.G., Dworski, J.G., 1997. Acoustic mapping of diffuse flow at a seafloor hydrothermal site: Monolith Vent, Juan de Fuca Ridge. *Geophysical research letters* 24(19), 2351-2354.
- Rona, P.A., Jones, C.D., 2009. Acoustic scintillation thermography. In Steele, J.H., Thorpe, S.A., Turekian, K.K., (Eds), *Encyclopedia of Ocean Sciences*, Academic Press, Oxford, 71-74, <http://dx.doi.org/10.1016/B978-012374473-9.00735-9>.
- Rona, P.A., Palmer, D.R., Jones, C., Chayes, D.A., Czarnecki, M., Carey, E.A., Guerrero, J.C., 1991. Acoustic imaging of hydrothermal plumes, East Pacific Rise, 21° N, 109°W, *Geophys. Res. Lett.* 18, 2233-2236.
- Rona, P.A., Trivett, D.A., 1992. Discrete and diffuse heat transfer at ASHES vent field, Axial Volcano, Juan de Fuca Ridge. *Earth and Planetary Science Letters* 109(1), 57-71.
- Santilli, K., Bemis, K., Silver, D., Dastur, J., Rona, P., 2004. Generating realistic images from hydrothermal plume data. In *Proceedings of the conference on Visualization'04*. IEEE Computer Society, 91-98.
- Sheng, J., Hay, A.E., 1988. An examination of the spherical scatterer approximation in aqueous suspensions of sand. *The Journal of the Acoustical Society of America* 83(2), 598-610.
- Silver, D., Wang, X., 1996. Volume Tracking. In *Proceedings of IEEE Visualization '96*, pp. 157-164, San Francisco, Ca, October 1996.
- Silver, D., Zabusky, N., 1993. Quantifying visualizations for reduced modeling in nonlinear science: Extracting structures from datasets, *J. Visual Comm. and Image Representation*, 4 (1), 46-61.
- Smart, C. J., Roman, C., Carey, S. N., 2013. Detection of diffuse seafloor venting using structured light imaging. *Geochemistry, Geophysics, Geosystems* 14(11), 4743-4757.
- Sundar, H., Silver, D., Gagvani, N., Dickinson, S., 2003. Skeleton based shape matching and retrieval. In *Shape Modeling International 2003*, IEEE, 130-139, doi: 10.1109/SMI.2003.1199609.
- Thomson, R. E., Subbotina, M. M., Anisimov, M.V., 2009. Numerical simulation of mean currents and water property anomalies at Endeavour Ridge: Hydrothermal versus topographic forcing, *J. Geophys. Res.* 114, C09020, doi:10.1029/2008JC005249.
- Viers, S.R., McDuff, R.E., Stahr, F.R., 2006. Magnitude and variance of near-bottom horizontal heat flux at the Main Endeavour hydrothermal vent field. *Geochemistry, Geophysics, Geosystems G3*, 7(2), doi:10.1029/2005GC000952.
- Xu, G., Di Iorio, D., 2011. The relative effects of particles and turbulence on acoustic scattering from deep-sea hydrothermal vent plumes. *The Journal of the Acoustical Society of America* 130(4), 1856-1867.
- Xu, G., Di Iorio, D., 2012. Deep sea hydrothermal plumes and their interaction with oscillatory flows. *Geochemistry, Geophysics, Geosystems*, 13(9), Q0AJ01, doi:10.1029/2012GC004188.
- Xu, G., Jackson, D., Bemis, K., and Rona, P., 2013. Observations of the volume flux of a seafloor hydrothermal plume using an acoustic imaging sonar, *G-cubed*, 14(7), 2369-2382.
- Xu, G., Jackson, D.R., Bemis, K.G., and Rona, P.A., 2014). Time series measurement of hydrothermal heat flux at the Grotto mound, Endeavour Segment, Juan de Fuca Ridge, *Earth and Planetary Science Letters* 404, 220-231, 2014.
- Wan, M., Dachille, F., Kaufman, A., 2001. Distance-field based skeletons for virtual navigation. In *Proceedings of the conference on Visualization'01*. IEEE Computer Society, 239-246.
- Walker, S.L., Baker, E.T., 1988. Particle-size distributions within hydrothermal plumes over the Juan de Fuca Ridge. *Marine geology* 78(3), 217-226.
- Weston, D. E., 1959. Observations on a scattering layer at the thermocline. *Deep Sea Research (1953)* 5(1), 44-50.

Figure Captions

Figure 1. (A) An active sonar sends out sound (transmitter); sound is scattered in multiple directions by scatterers (target) which may be particles or small scale sound speed or density anomalies. Sound scattered in the direction of the sonar (backscattered) is measured as the signal (receiver). (B-D) A comparison of the sonar configurations for submersible, remote operated vehicle and cabled observatory. Vehicles (and tripod) are not to scale with sonar and rotational motors.

Figure 2. (A) A horizontal cross-sectional profile of the volume backscatter cross-section (σ_b) measured by COVIS from a hydrothermal plume discharging from the Grotto mound, Endeavour Segment, Juan de Fuca Ridge indicates the range of observed backscattering strengths. The horizontal cross-section is at approximately 6 m above the mound. The backscatter dataset was recorded on Jan 22nd, 2014 at 22 hours UTC Time. (B) Models predict backscattering strengths based on the assumption of scattering mechanisms (particles or temperature fluctuations). The observed backscattering strengths are indicated for the two calibrated sonars (SM2000 and COVIS). Ocean Networks Canada Data Archive, <http://www.oceannetworks.ca>, COVIS data from 22 Jan 2014, Oceans Networks Canada, University of Victoria, Canada. Downloaded 23 Jan 2014.

Figure 1. As results of the first deliberate acoustic imaging, these two successive acoustic images taken at Clam Acres (EPR 21°N) using the Mesotech sonar already show the changing bending of hydrothermal plumes in response, presumably, to changes in ocean currents. These images also highlight the merging of plumes from two separate black smokers. (A) Acoustic image at 20:24 11-20-1990. (B) Acoustic image at 21:11 11-20-1990. Data acquired using the Mesotech 971 on DSV Turtle.

Figure 2. (A) This acoustic image was computed as pings summed pairwise as complex signals and magnitudes averaged over the pairs. (B) The same data set was instead computed with pings differenced pairwise as complex signals and magnitudes averaged over the pings. The differenced ping image appears cleaner and clearly shows three distinct plumes. The raw data were acquired using COVIS and the NEPTUNE observatory on Oct 26, 2011 at 12:00 GMT. In both (A) and (B) the isosurfaces are set at -55 dB (blue), -65 dB (cyan), and -75 dB (orange but appears green due to overlying isosurfaces). The seafloor is shown as a grey shiny surface; bathymetry from Clague et al. (2008). Yellow dots show the positions of NEPTUNE sensors COVIS, RAS, and BARS at (0,0,0), (-4,-12,15), and (-7,-10,12) respectively; RAS and BARS positions are approximate.

Figure 3. Visualizing 3D acoustic data involves such volume visualization techniques as (A) layering partially transparent isosurfaces, (B) ray-tracing, and (C) fitting arbitrary shapes. The data set displayed here was collected on 11-20-90 at 20:24 GMT using the Mesotech setup on DSV Turtle.

Figure 4. The quantification process starts with the extraction of the plume from the background data (A) and continues with the estimation of a centerline (B-C) and slice-wise computation of plume properties (D-E). The centerline can be defined by (and then computed from) the isosurface shape (B), locations of global maxima (C). Plume properties such as radius (D) and dilution (E) are inherently dependent on the isosurface threshold. Data were acquired on 11-20-90 at 21:11 GMT using the Mesotech setup on DSV Turtle.

Figure 5. (A) Acoustic image of the plume and sulfide structure at Monolith, Cleft segment, Juan de Fuca ridge, on 10 Sept 1996 at 19:15 showing the narrowing of the isosurface before expansion. Data were acquired using the Mesotech 971 on the DSV SeaCliff. (B) The necking is even more apparent in the e-folding radius for this acoustic image and a second one made earlier the same day. (C) A cartoon illustrates the concept of multiple small plumes from individual black smokers merging to create a much

larger combined plume. The necking results from the excess momentum available in the merged plume.

Figure 6. (A) A volume based on a single (or the complex difference of two pings) acoustic ping at each elevation forms a picture much like a snapshot except that each elevation is exposed at a slightly different time over about 4 minutes. (B) The average of 6 such volumes collected successively is essentially a time-average of the plume and shows the classic expanding isosurface structure of a plume. The data were acquired on 25 Jul 2000 at 21:35 GMT using the Simrad SM2000 sonar on ROV Jason while imaging the plume above Grotto's North Tower.

Figure 7. (A) Two diffuse scans are partially overlaid to increase areal coverage. (B) Thresholding on the decorrelation intensity (product of decorrelation and backscatter intensity) highlights the areas with high decorrelation to be interpreted as regions of diffuse discharge. (C) Detected diffuse flow (blue) overlain on the topography around S&M in Main Endeavour Field on the Juan de Fuca Ridge. Data was collected in 2000 by Chris Jones and Paul Johnson using the Simrad SM2000 sonar.

Figure 8. (A-C) The geometric correction for line-of-sight velocity V_r to vertical velocity W relies on the assumptions that the horizontal velocity U is an effect of ocean currents outside the plume that only varies in the vertical direction and that the velocity at a given point on the centerline (V_c) is parallel to the centerline. (D) An example slice of the estimated vertical velocity from COVIS data acquired in May 2011 shows a rough bull's-eye pattern typical of a time-averaged plume modified by internal eddies.

Figure 9. (First row) Cartoon of plumes bending in the changing currents emphasize the asymmetry and periodicity of tidally-driven bending. (Second row) Selected time steps from the first 24-hour time series of acoustic images of a hydrothermal plume. Data acquired using the Simrad sonar in July 2000.

Figure 10. Models of how hydrothermal plumes rise based on theory presented in Kaye and Linden (2004). The isosurfaces of velocity for (A) two plumes merging or (B) five plumes merging both show the expansion of the initial plumes the necking together of the plumes as they merge and the eventual expansion of the combined plume. (C) Extracting the vertical velocity data for the five plume merging model shows how the initial velocities in the plumes (cyan and black lines) match simple plume theory for a single vent (red dotted line), but as they merge the velocity increases (black and cyan lines) to the simple plume theory prediction for the equivalent to five vents (pink dash-dot line).

Figure 11. (A) A close-up of the sonar head on (B) COVIS. (C) COVIS (orange cylinder) is deployed just NE of Grotto in the Main Endeavour Field on the Juan de Fuca Ridge and connected to a junction box south of Grotto (yellow trapezoid) as are other instruments sited on the north end of Grotto (green pyramid). Bathymetry from Clague et al., 2008.

Figure 12. This is a summary of the first month of COVIS data for the largest of the Grotto plumes. (First row) The north-south and east-west components of the plume orientation show a strong periodicity (which spectral analysis confirms is ~2 cycles/day). There are also some intervals where the plume orientation is changing more complexly or is constant. The bending components are the distance the plume at an arbitrary height (10 m) is offset from its base. (Second row) Vertical velocity from the corresponding Doppler data shows less periodicity as there are fewer estimates/day in general. Semi-diurnal periodicity is less pronounced in the Doppler data sets, which were collected with the same frequency (~3 hrs) but just after (~20 min) the Imaging data sets. (Third row) Estimated area of diffuse discharge for all of Grotto visible to COVIS is highly variable. (Fourth row) Temperatures for a black smoker (BARS data) and a diffuse flow patch (RAS data) on Grotto both show strong semi-diurnal periodicity. Ocean Networks Canada Data Archive, <http://www.oceannetworks.ca>, COVIS, BARS and RAS data from 29 Sept 2010 to 26 Oct 2010, Oceans Networks Canada, University of Victoria, Canada. Downloaded on 1 Jan 2013 or earlier for COVIS data.

Figure 13. (A) and (C) represent two time steps in a time series of plume images after the plumes have

been extracted from the background. Red arrows indicate the tracking correspondence. (B) and (D) show the corresponding skeletons for the plumes in the two time steps. (E) and (F) define one particular classification scheme for plume bending. Each state represents a particular phase of the expected tidal cycle. Acoustic data acquired 29 Sept 2010 using COVIS. Ocean Networks Canada Data Archive, <http://www.oceannetworks.ca>, COVIS data from 29 Sept 2010, Oceans Networks Canada, University of Victoria, Canada. Downloaded on 30 Sept 2010.

Figure 14. An analysis of the first month of COVIS data acquired in October 2010 through the Ocean Networks Canada's NEPTUNE observatory. Each acoustic image is assigned to a particular bending classification P1 to P5 (whose description in words is also given (D))and its incidence noted in the time line (A). All instances in a given category are averaged to produce a typical plume visualization for that category (C). The periodicity of each category indicates a tidal driven system (B).

figure 1

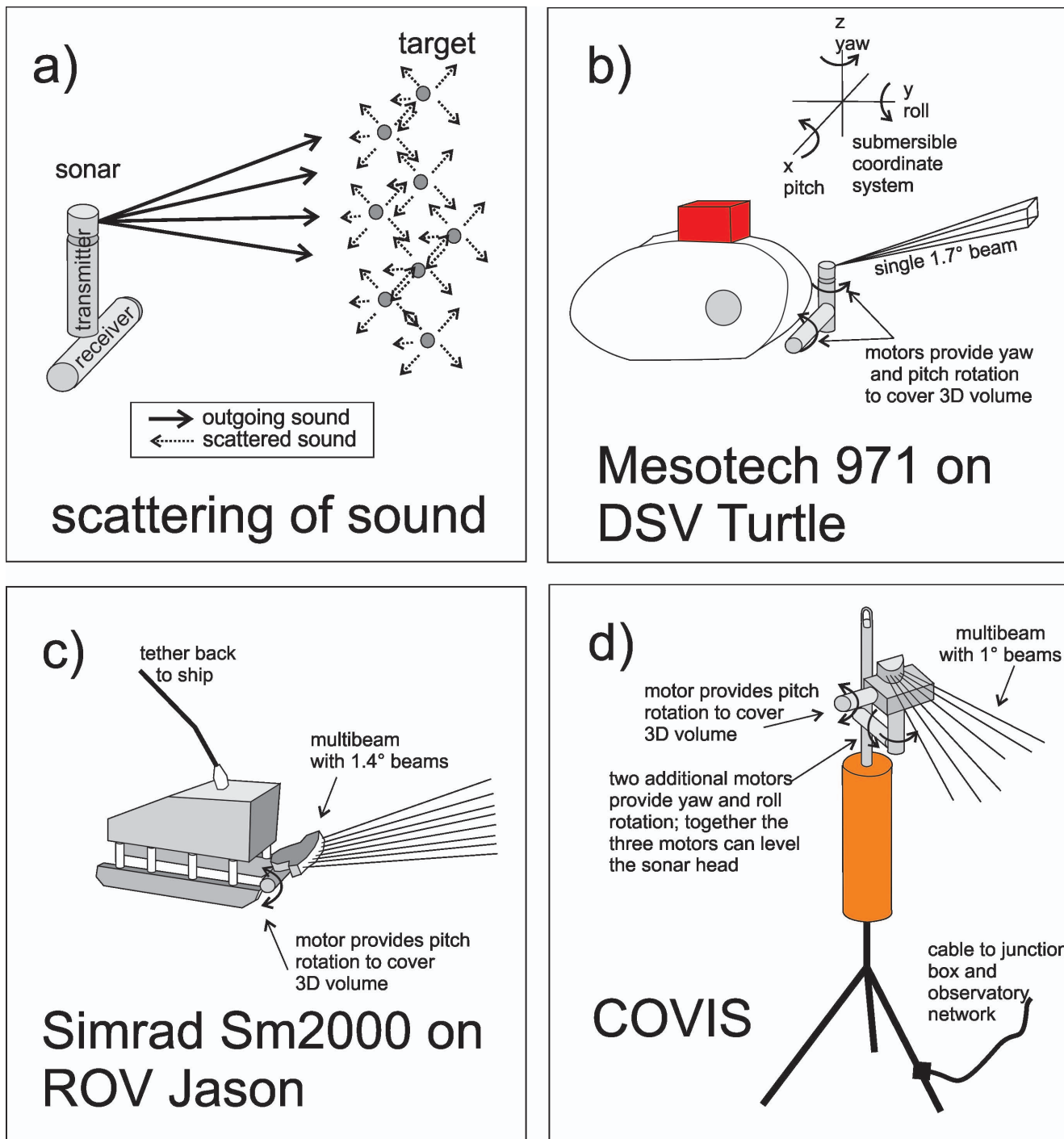


figure 2

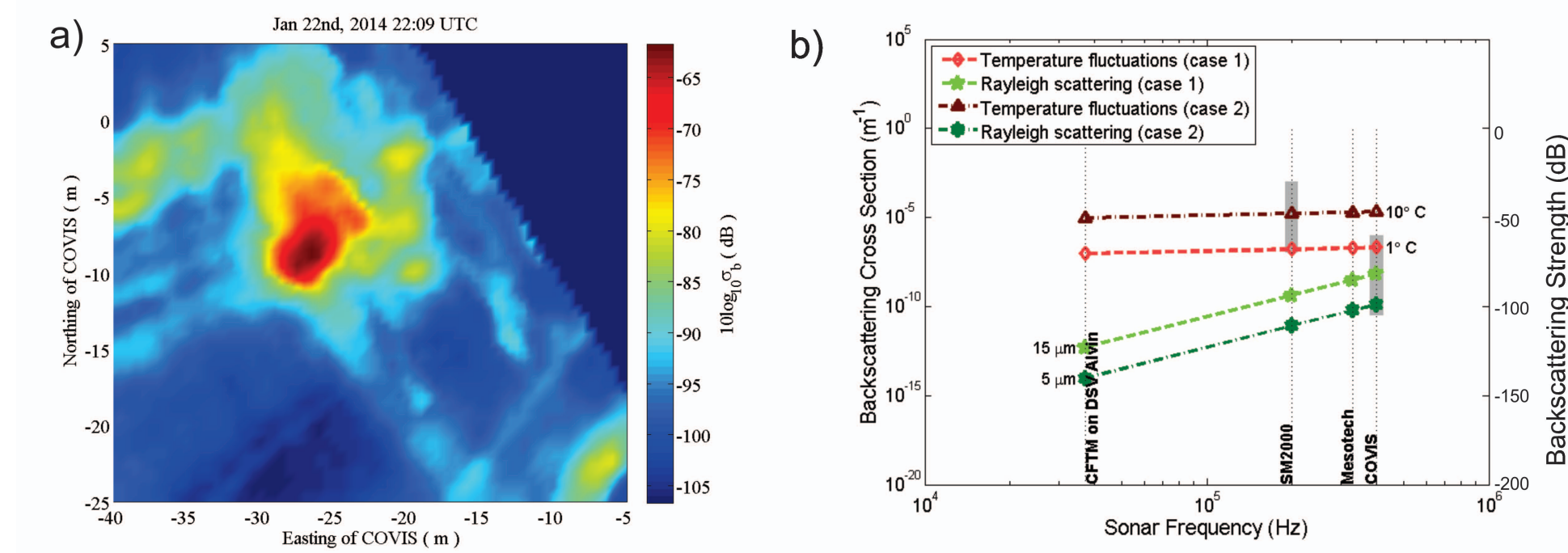


figure 3

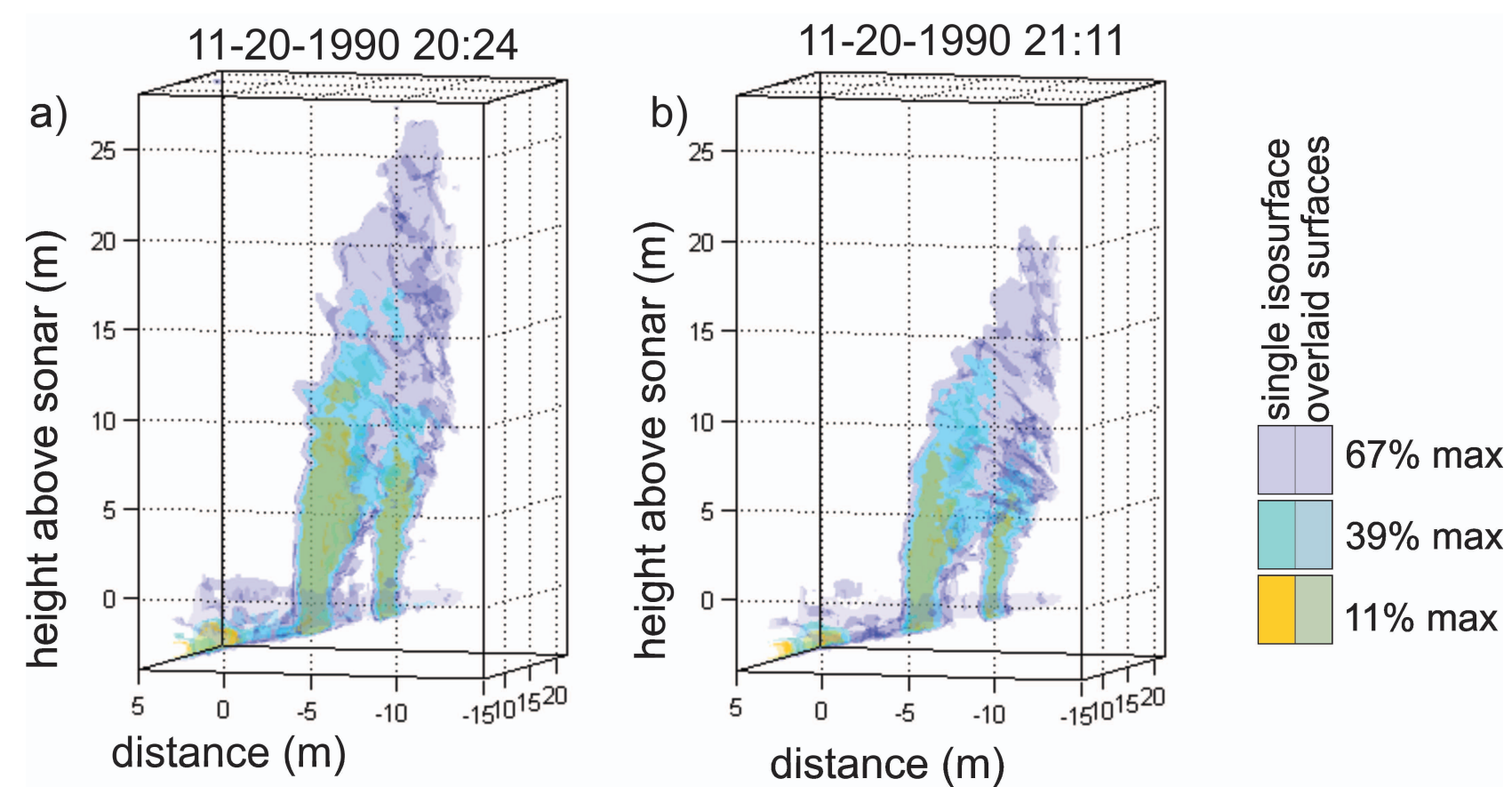


figure 4

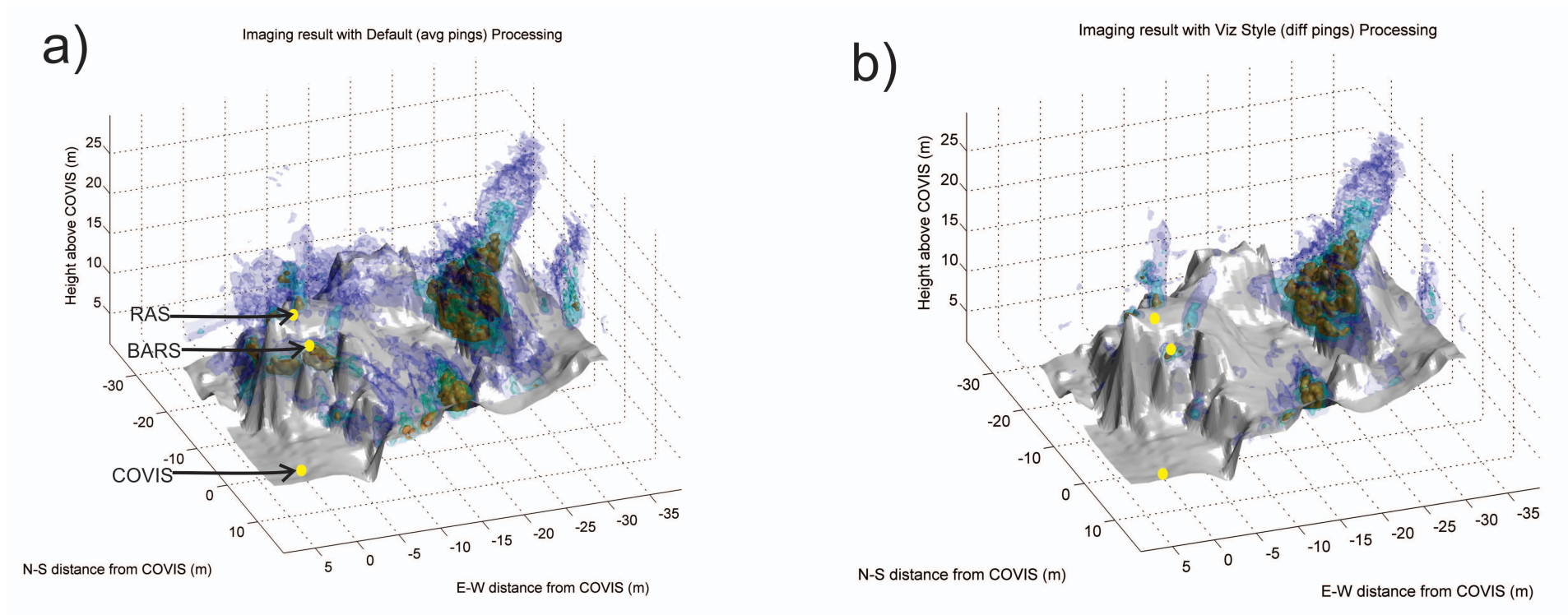


figure 5

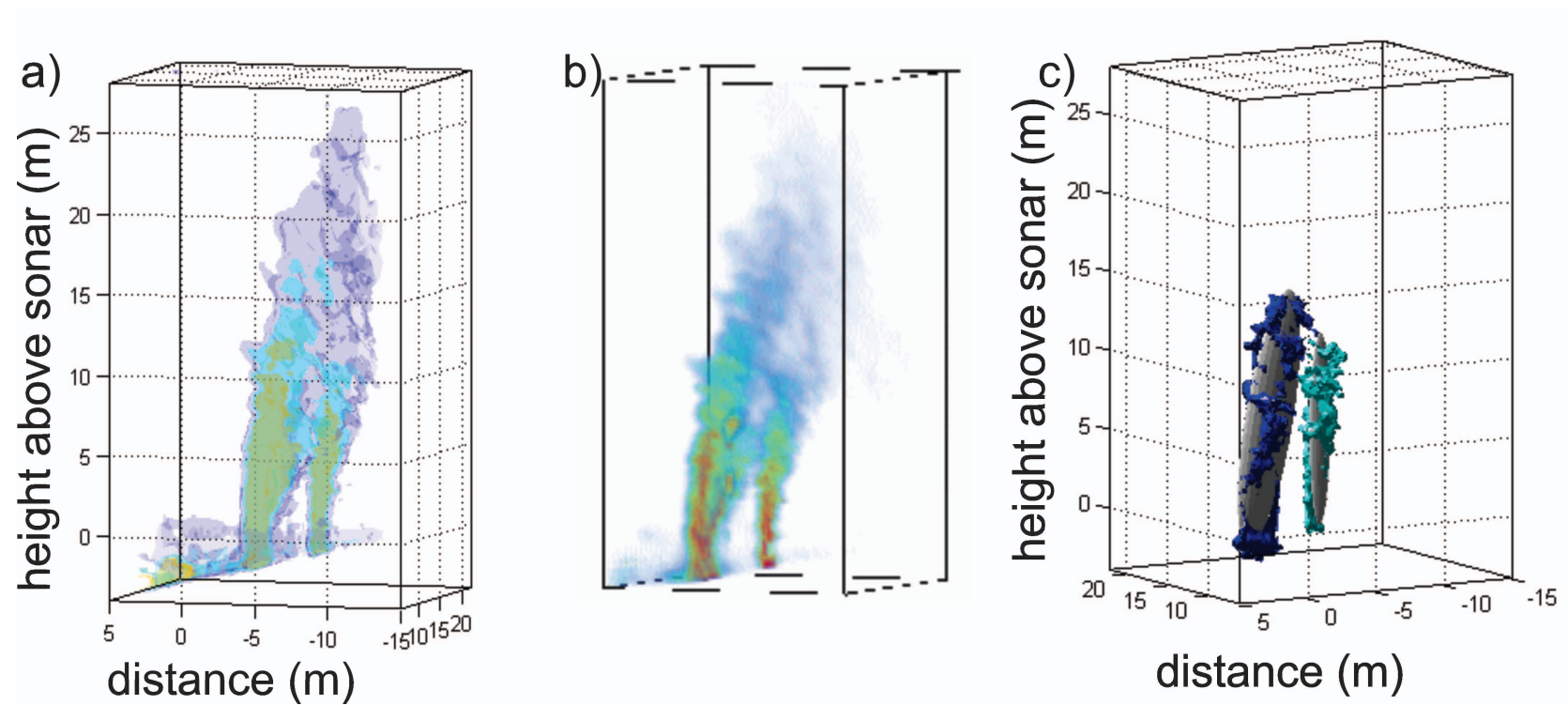


figure 6

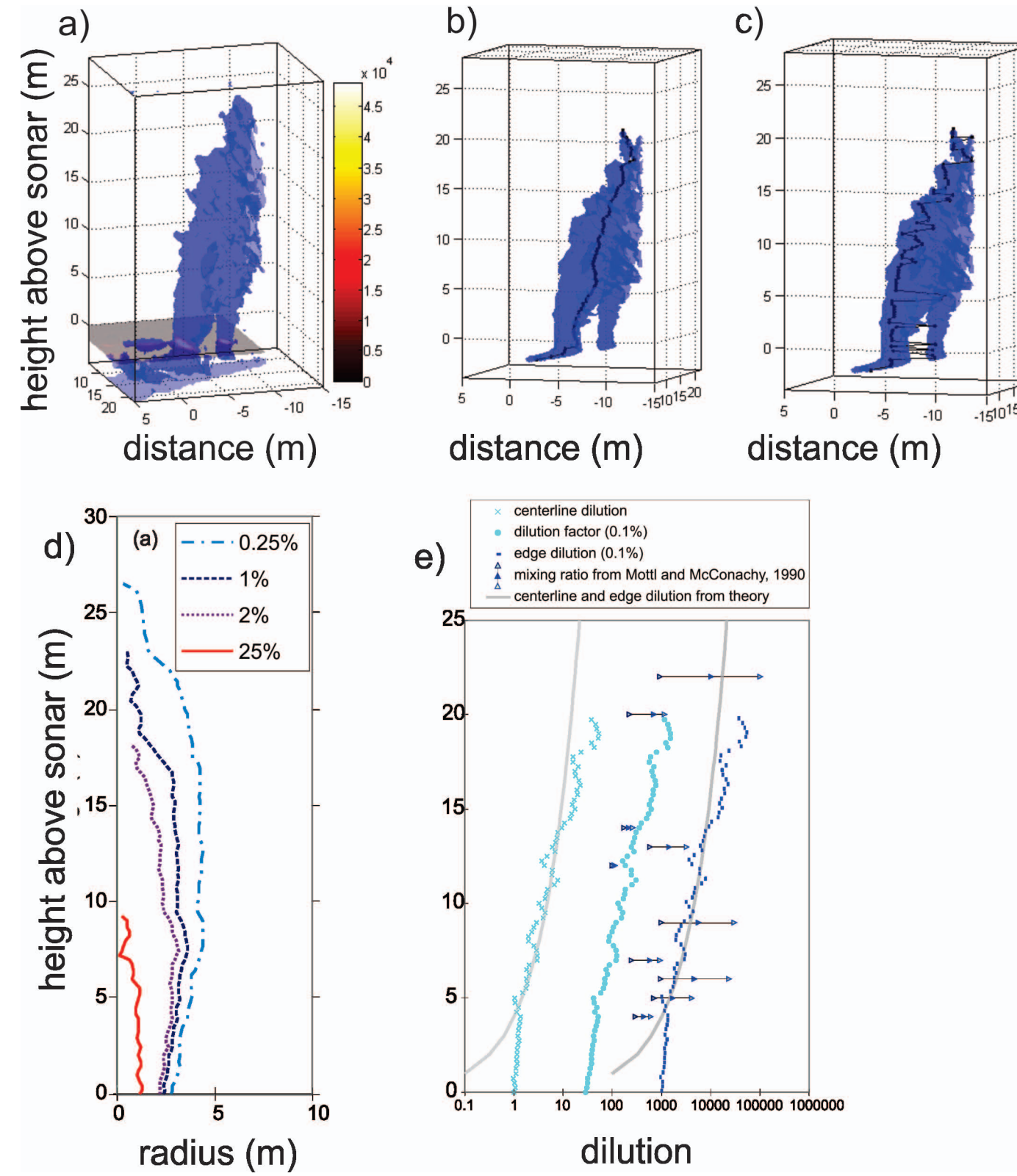


figure 7

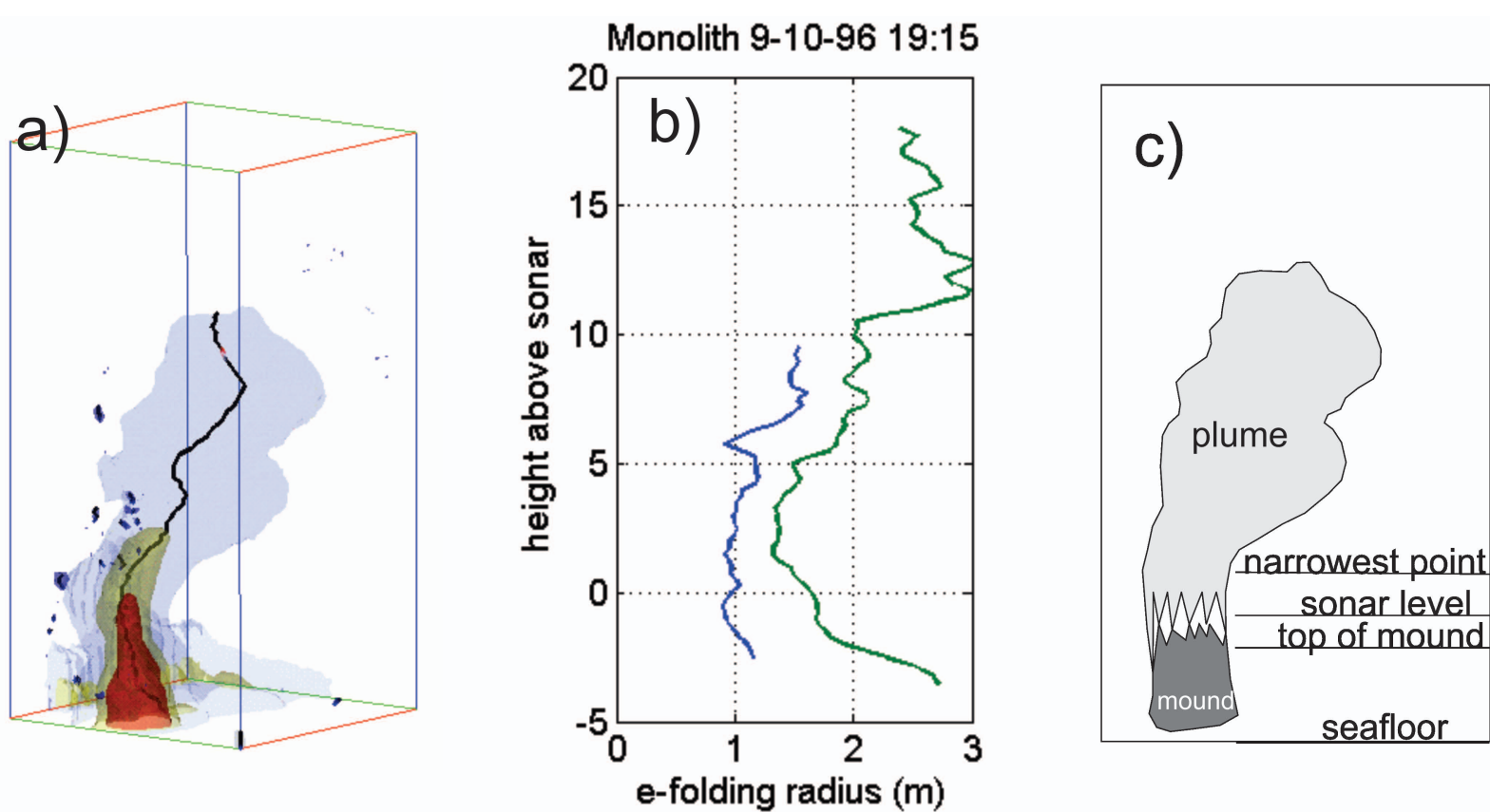


figure 8

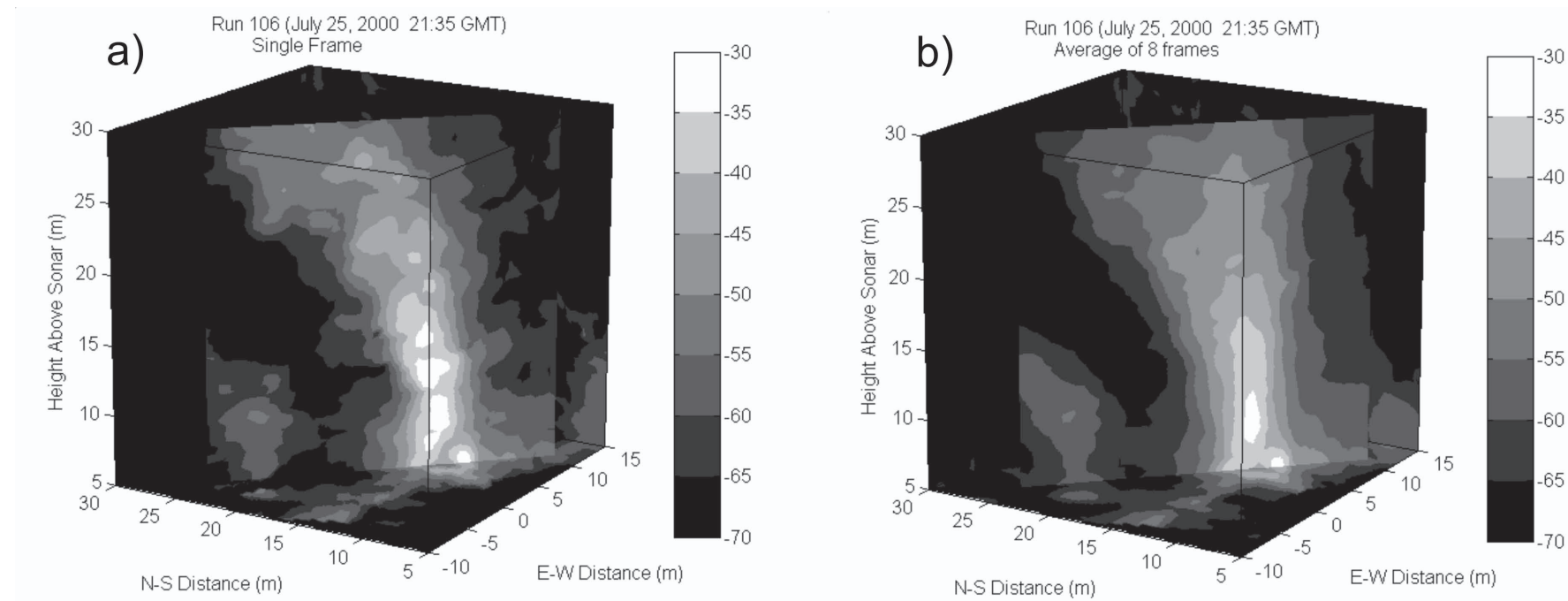


figure 9

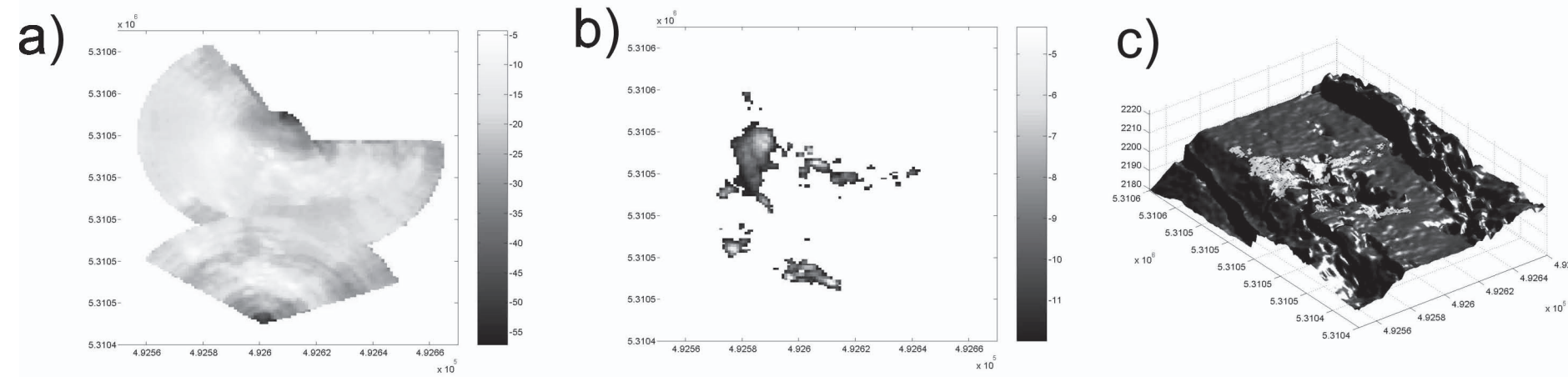


figure 10

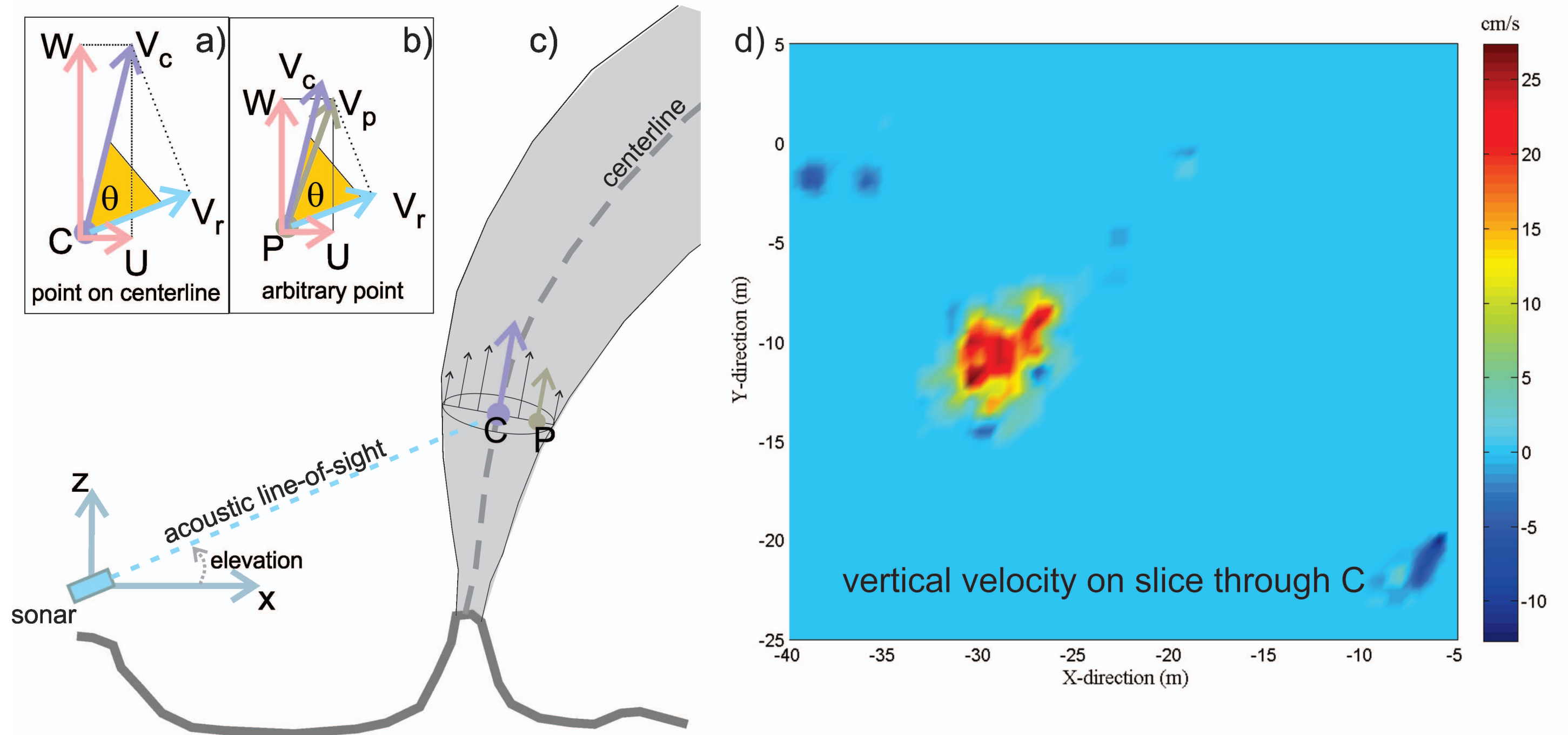


figure 11

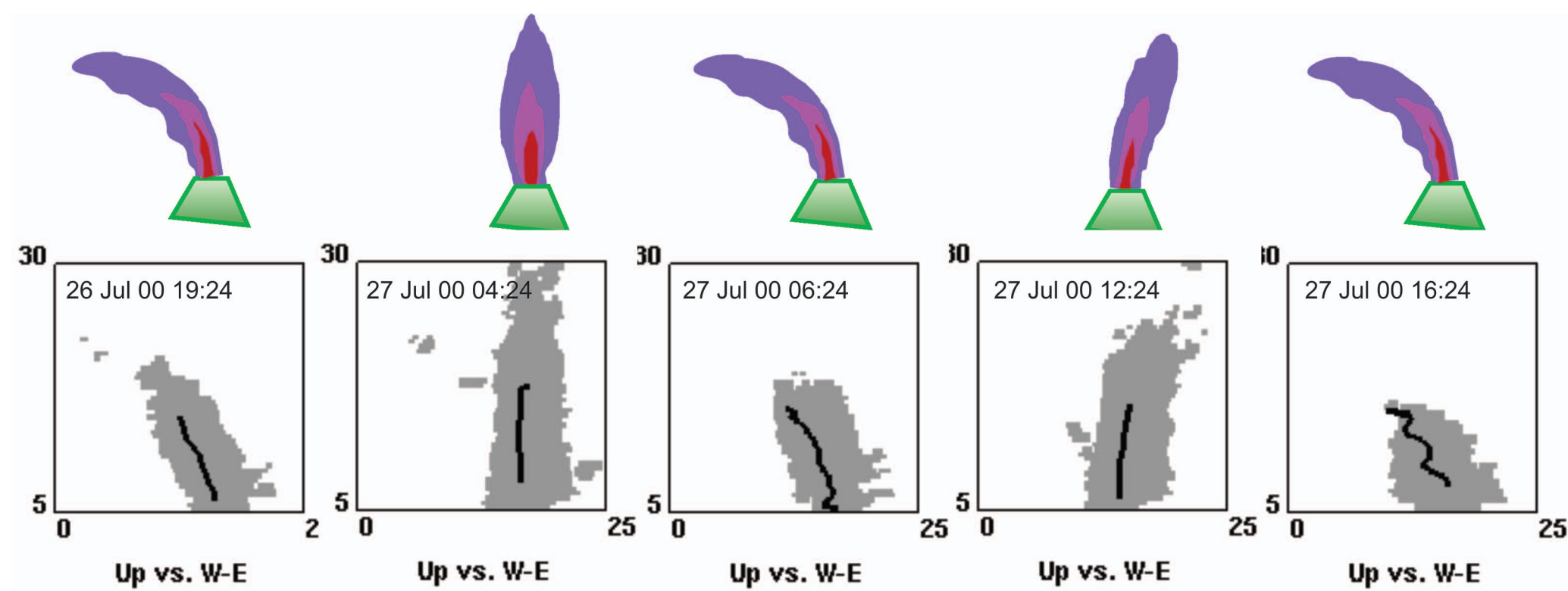


figure 12

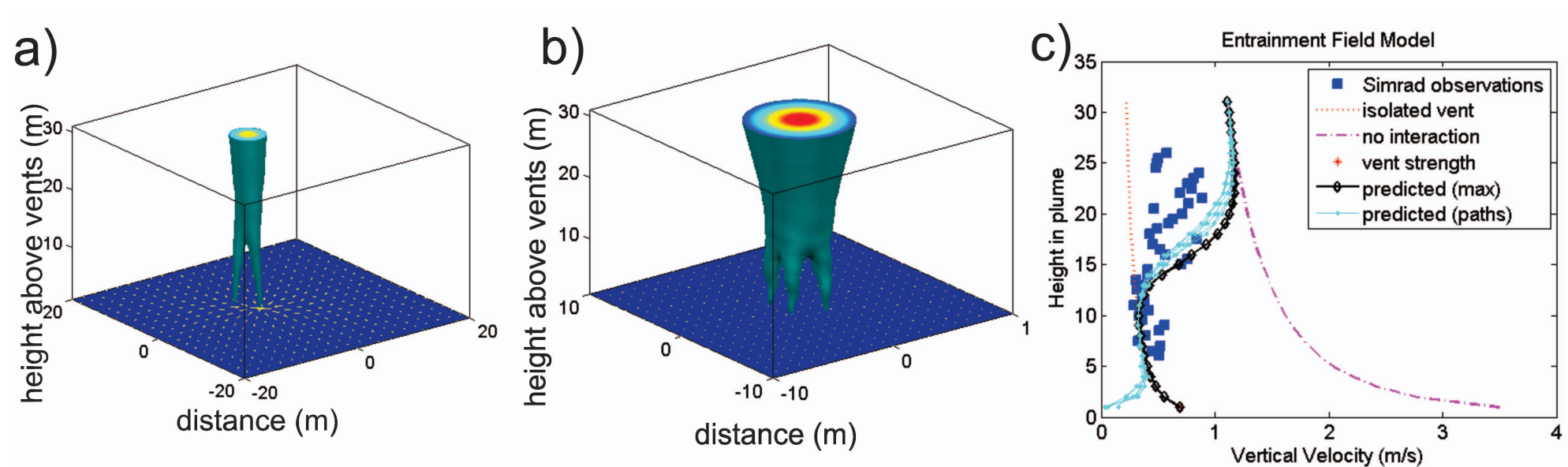


figure13

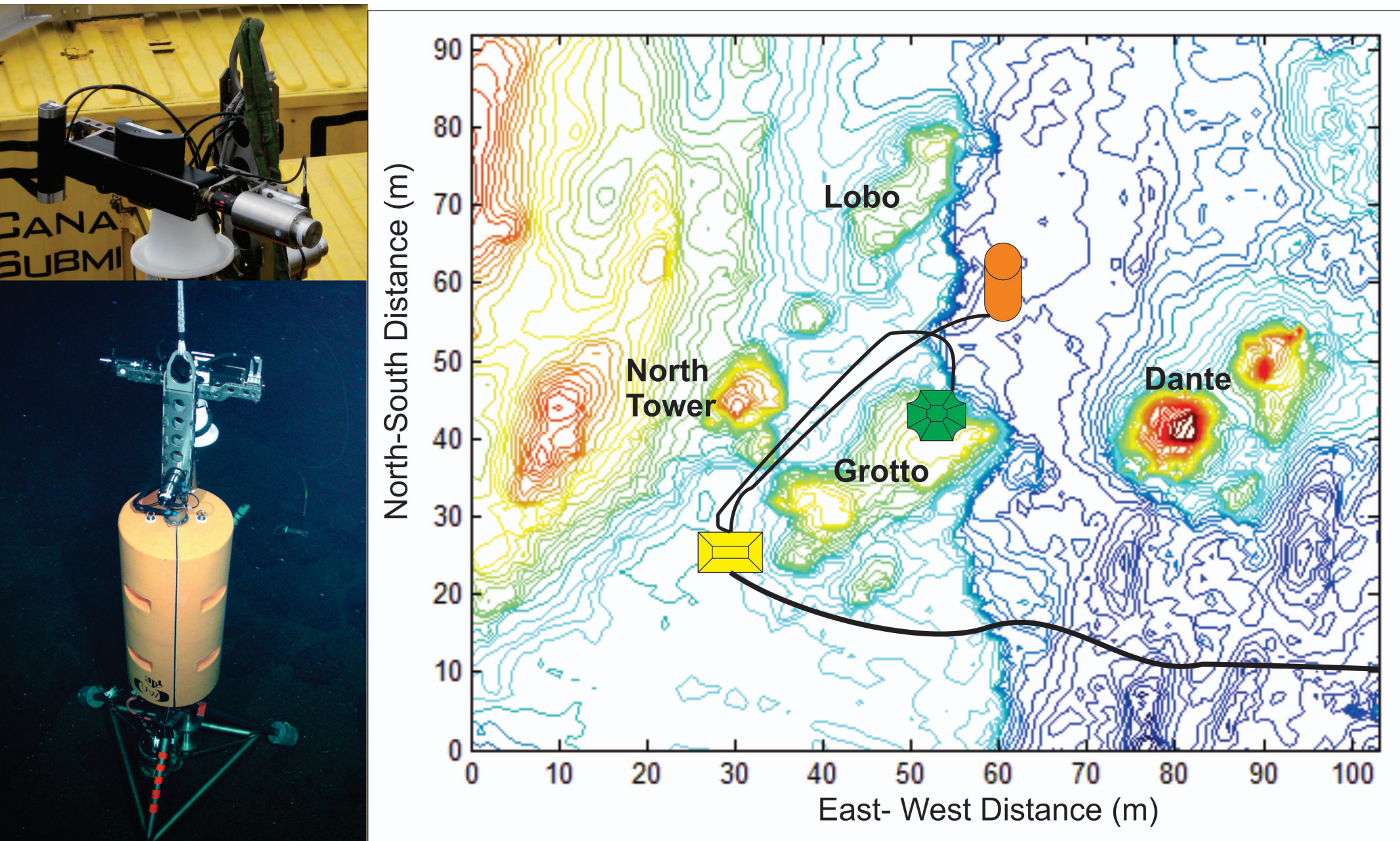


figure 14

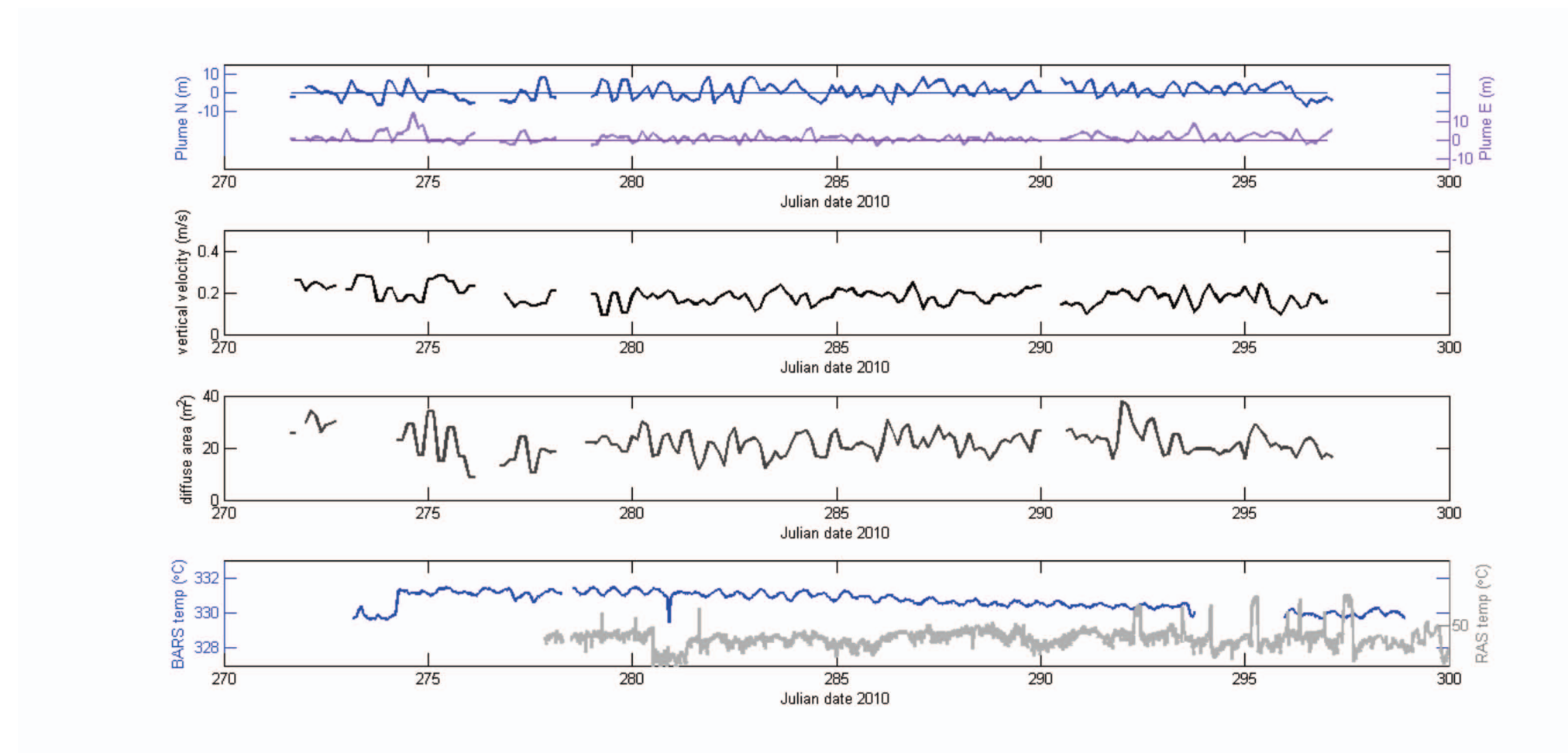


figure 15

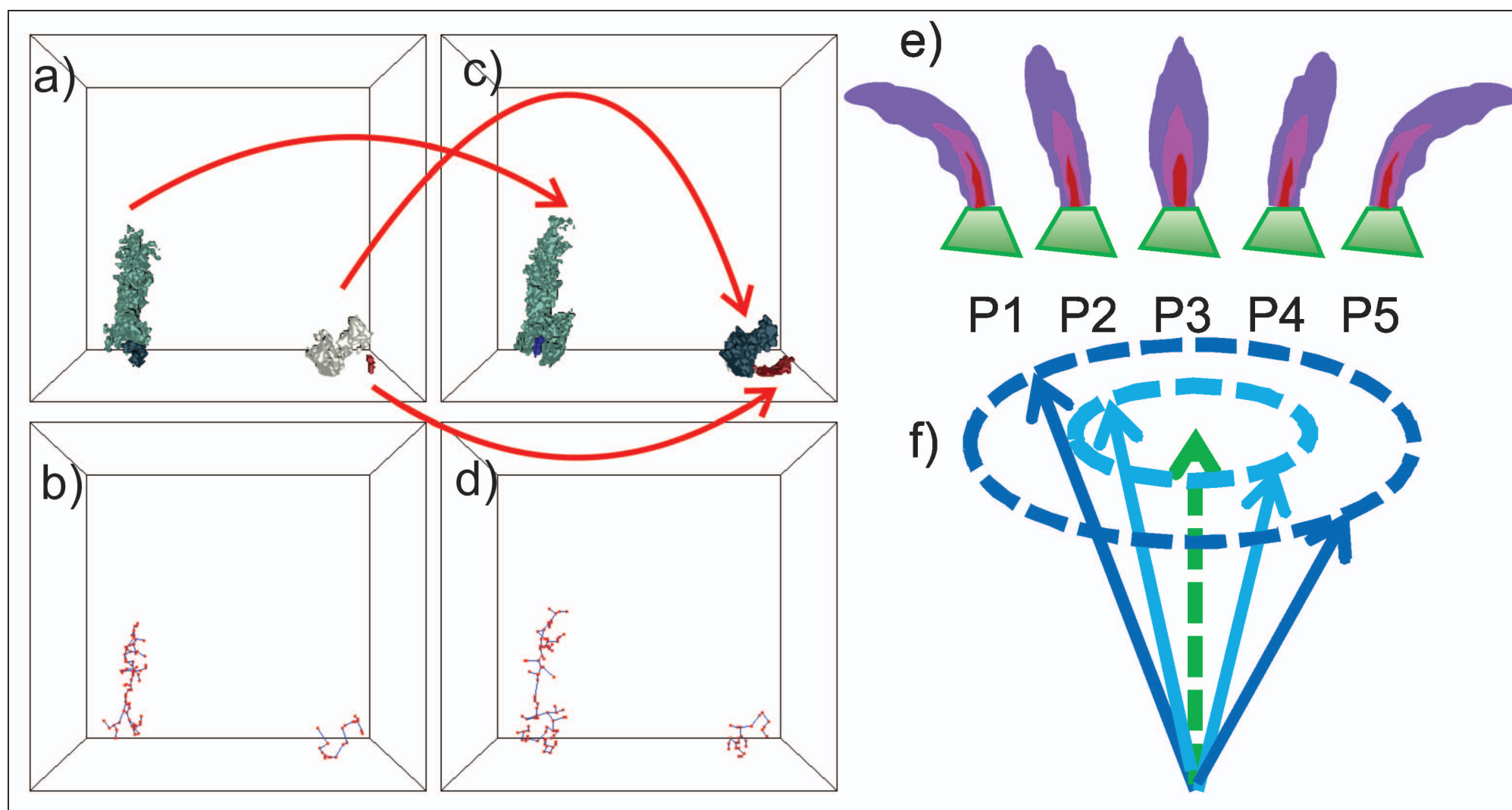


figure 16

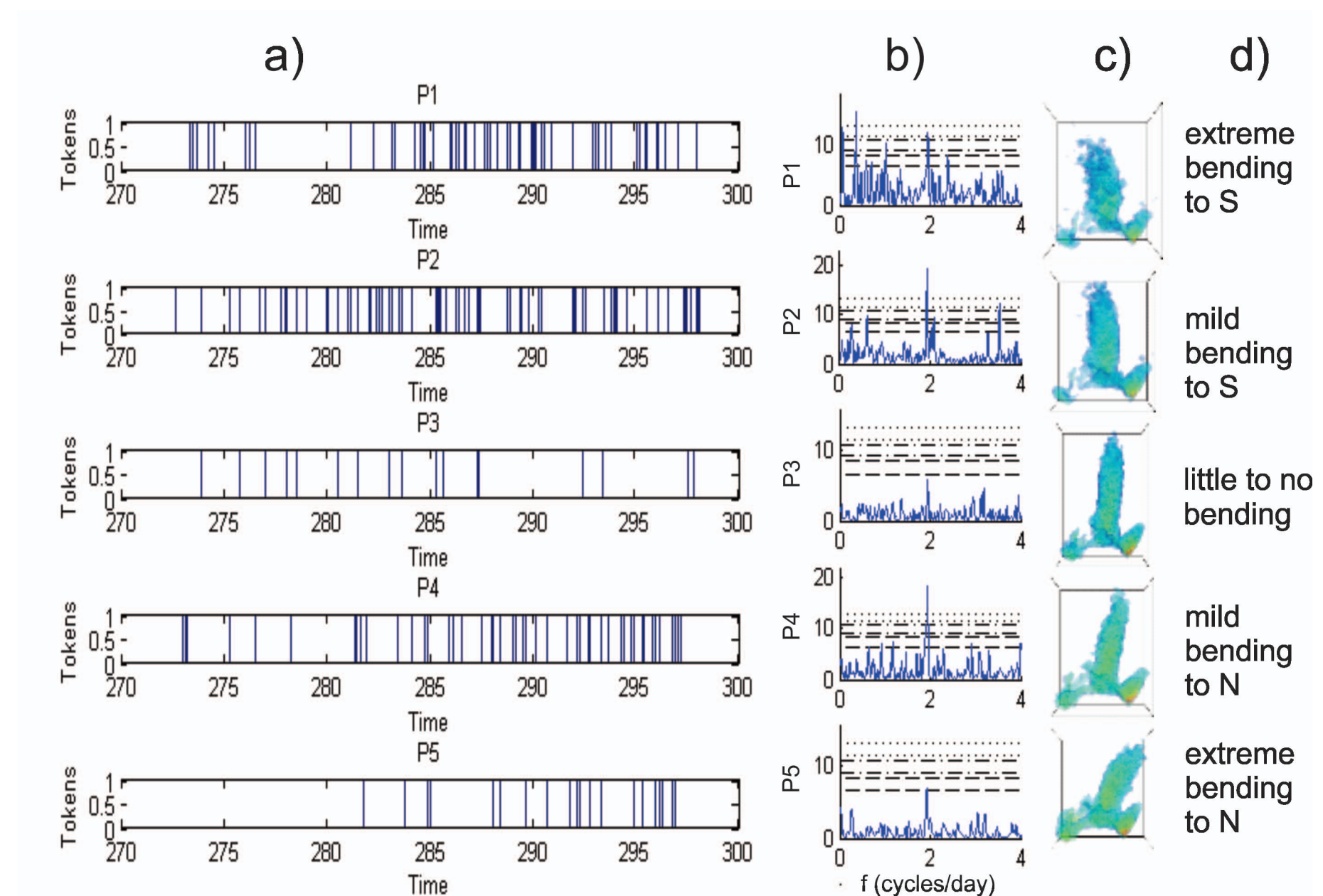


Table 1. Major landmarks in the development of acoustic imaging for hydrothermal flow regimes.

Year*	Landmark	Acoustic Technology	Visualization Methods	References*
1984	1 st detection of a hydrothermal plume	Range-finding sonar	Photo of sonar display	Palmer et al., 1986
1990	1 st plume image	Mechanical rotation of single narrow beam	Layered isosurfaces	Rona et al., 1991
1996	1 st detection of diffuse flow; Plume centerline and expansion rate quantified; eddy sizes estimated	Multibeam used; complex waveform recorded	Feature extraction; centerline estimation; ellipsoid fitting	Rona et al., 1997; Rona et al., 1998; Bemis et al., 2000; Bemis et al., 2002; Rona et al., 2002
2000	24 hr time series; 1 st vertical velocities; 1 st evidence for tidal driving of entrainment rates; diffuse flow mapping	Ping differencing for imaging; Doppler mode enabled; initial methods of decorrelation processing for diffuse mode	Volume rendering; skeletons for centerlines	Jackson et al., 2003; Santilli et al., 2004; Rona et al., 2006; Rona and Jones, 2010
2010	Long-term monitoring starts; confirmation of tidal driving of entrainment rates; 1 st remote heat flux estimates	Adaptation to observatory; Methods for volume flux and heat flux estimation	Feature tracking; event detection	Rona and Light, 2011; Xu et al., 2013; Xu et al., 2014; Bemis et al., 2014; Ozer et al., 2014

*Year in which the acoustic data was collected. References refer to when the acoustic results or application thereto was published; some techniques (especially in visualization) were previously published.

Table 2 Sonar setup details for acoustic imaging

Sonar	Carrier frequency	Pulse length	Effective beam resolution ^a	Transmit Source Level	Sampling frequency	Signal recorded	Year used	Vehicle	Imaging site	Key References
CTFM	37 kHz	n/a	n/a	unknown	n/a	Photo of scan	1984	HOV Alvin	EPR 11°N	Palmer et al, 1986
Mesotech 971 with conical beam	330 kHz	100 us = 0.1 ms	1.7° x 0.9°	220 dB	10 kHz or 20 kHz	magnitude	1990	DSV Turtle	EPR 21°N, Clam Acres	Rona et al., 1991; Rona et al., 1998
Mesotech 971 with conical beam	330 kHz	100 us	1.7° x 0.9°	220 dB		complex	1996	DSV Seacliff	JdFR, Cleft, Monolith	Rona et al., 1997; Bemis et al., 2002
Simrad SM2000	200 kHz	Variable (1.2 ms for Doppler)	1.4° x 1.4° (multi-beam)		20000 Hz	complex	2000	ROV Jason	JdFR, Endeavour, MEF, various	Jackson et al., 2003; Santilli et al., 2004 Bemis et al., 2006; Rona et al., 2006
Reson Seabat 7125	400 kHz (or 200 kHz for diffuse)	Variable (0.5 ms imaging; 1.5 ms Doppler; 0.3 ms diffuse)	1° x 0.5° (multi-beam)	Variable (220 dB imaging and Doppler; 200 dB diffuse)	34483 Hz	complex	2010-present	NEPTUNE cabled observatory	JdFR, Endeavour, MEF, Grotto	Rona and Light, 2011; Xu et al., 2012 Xu et al., 2014

^aEffective beam resolution considers the actual beam width (vertical or conical), azimuthal resolution (especially for multi-beams) and elevation step size (which may be greater than or equal to the vertical beam width). The first number is the vertical resolution, and the second is the horizontal or azimuthal resolution. Pulse length and sampling frequency control resolution along the beam.

Table 3. Acoustic and visualization processing sequence for three sonar modes

	Imaging	Doppler	Diffuse
In sonar/control	Filtering Packaging	Filtering Packaging	Filtering Packaging
Processing for each ping separately	Phase Correction Filtering Beamforming Calibration	Phase Correction Filtering Beamforming Calibration	Phase Correction Beamforming Calibration Filtering
Collective processing for a group of pings	Differencing/Averaging (Fig. 4) Gridding & Time Averaging (Fig. 8)	Doppler Shift Geometric Correction (Fig. 10) Gridding	Ping-to-Ping Correlation Gridding
Visualization	Layered Isosurfaces (Fig. 3-8) Volume Rendering (Fig. 5)	Slices (Fig. 10), Isosurfaces, Time Series Graphs	Correction for Bathymetry Drape on Surface (Fig. 9)
Property Extraction	Feature Extraction (Fig. 5-6) Centerline Estimation (Fig. 6) Plume Properties (Fig. 6-7)	Flux Computations	Threshold Application Patch Isolation Area Estimation
Time Series Analysis	Feature Tracking (Fig. 15-16) Event Detection (Fig. 15-16) Spectral Analysis (Fig. 16)	Spectral Analysis	Spectral Analysis